Red Galaxies at High Redshift

Wuyts, S.E.R.

Citation

Wuyts, S. E. R. (2007, September 27). *Red Galaxies at High Redshift*. Retrieved from https://hdl.handle.net/1887/12355

Chapter 7

Color distributions, number and mass densities of massive galaxies at $1.5 < z < 3$: comparing observations with merger simulations

Abstract. We present a comparison between the observed color distribution, number and mass density of massive galaxies at $1.5 < z < 3$ and a model by Hopkins et al. that relates the quasar and galaxy population on the basis of gas-rich mergers. In order to test the hypothesis that quiescent red galaxies are formed after a gas-rich merger involving quasar activity, we confront photometry of massive ($M > 4 \times 10^{10}\ M_{\odot}$) galaxies extracted from the FIRES, GOODS-South, and MUSYC surveys, together spanning an area of 430 arcmin^2, with synthetic photometry from hydrodynamical merger simulations. The merger simulations are placed in a cosmological context using the observed quasar luminosity function. We find that the synthetic $U - V$ and $V - J$ colors of galaxies that had a quasar phase in their past match the colors of observed galaxies that are best characterized by a quiescent stellar population. The model predicts a number density of quiescent red galaxies with $M > 4 \times 10^{10}\ M_{\odot}$ of $3.6 \pm 0.6 \times 10^{-4}$ Mpc^{-3} at $z \sim 1.9$ and $1.0 \pm 0.2 \times 10^{-4}$ Mpc^{-3} at $z \sim 2.6$, while the observations amount to $2.3^{+0.8}_{-0.6} \times 10^{-4}$ Mpc^{-3} at $z \sim 1.9$ and $1.3^{+0.6}_{-0.4} \times 10^{-4}$ Mpc^{-3}. The corresponding mass densities are $4.4 \pm 0.6 \times 10^{7}\ M_{\odot}$ Mpc^{-3} at $z \sim 1.9$ and $1.3 \pm 0.3 \times 10^{7}\ M_{\odot}$ Mpc^{-3} at $z \sim 2.6$ for the model against $2.9^{+1.0}_{-0.7} \times 10^{7}\ M_{\odot}$ Mpc^{-3} at $z \sim 1.9$ and $2.0^{+0.9}_{-0.6} \times 10^{7}\ M_{\odot}$ Mpc^{-3} for the observations. Hence, the data are consistent with the models in which every quiescent massive galaxy underwent a quasar phase in the past. The merger model also predicts a large number and mass density of galaxies undergoing star formation driven by the merger. We find that the number and mass density is consistent with the observations of star-forming galaxies. However, their colors do not match those of observed star-forming galaxies. In particular, the colors of dusty red galaxies are not reproduced by the simulations. Several possible origins of this discrepancy are discussed, ranging from the method to compute the model predictions to the validity of the model assumptions to physical mechanisms such as a large-scale wind producing a foreground screen of obscuring material and thus leading to more efficient reddening.

S. Wuyts, T. J. Cox, N. M. Förster Schreiber, M. Franx, L. Hernquist,
P. F. Hopkins, I. Labbé, B. Robertson, G. Rudnick, S. Toft & P. G. van Dokkum

7.1 Introduction

In recent years, deep near- and mid-infrared observations have revealed significant populations of red galaxies at redshifts $z \sim 2$ and above (Franx et al. 2003; Daddi et al. 2004; Yan et al. 2004). The population of Distant Red Galaxies (DRGs), selected by the simple observed color criterion $J - K > 2.3$, makes up 66% in number and 73% in mass of the $2 < z < 3$ galaxy population at the high-mass end ($M > 10^{11}\ M_{\odot}$, van Dokkum et al. 2006). Probing to lower masses, Wuyts et al. (2007) found that the lower mass galaxies at redshifts $2 < z < 3.5$ have bluer rest-frame $U - V$ colors compared to the most massive galaxies. A substantial fraction of the massive red galaxies at high redshift are best characterized by a quiescent stellar population on the basis of their broad-band SEDs (Labbé et al. 2005; Wuyts et al. 2007) and the presence of a Balmer/4000Å break and absence of emission lines in their rest-frame optical spectra (Kriek et al. 2006).

Any satisfying theory of galaxy formation has to account for the presence and abundance of these massive red galaxies in the early universe, a condition that was by no means met by the state-of-the-art hierarchical galaxy formation models at the time of their discovery (Somerville 2004).

In the meantime, merger scenarios involving AGN activity have been invoked by semi-analytic models (Granato et al. 2004; Croton et al. 2006; Bower et al. 2006; De Lucia & Blaizot 2007) and hydrodynamical simulations (Springel et al. 2005a; Di Matteo et al. 2005) to explain simultaneously the mass build-up of galaxies and the shutdown of star formation. Such an evolutionary scenario predicts an obscured (and thus red) starburst phase and ends with a quiescent (and thus red) remnant galaxy (e.g., Hopkins et al. 2006a). Observational support for the connection between dust-enshrouded starbursts, merging, and AGN activity from samples of nearby Ultra-Luminous Infrared Galaxies (ULIRGs) dates from as early as Sanders et al. (1988). Furthermore, the observed relation between the supermassive black hole (SMBH) mass and the mass (Magorrian et al. 1998) or the velocity dispersion (Ferrarese & Merritt 2000; Gebhardt et al. 2000) of their host suggests that black hole and galaxy growth are intimately connected. This scaling relation can be reproduced by merger simulations with implemented AGN feedback (Robertson et al. 2006).

Motivated by the observed and simulated correlations between the properties of SMBHs and their hosts, Hopkins et al. (2006b) used the observed quasar luminosity function to derive the galaxy merger rate as a function of mass. This chapter uses the merger rate function derived by this model in combination with hydrodynamical SPH simulations to predict the color distribution, number and mass density of massive galaxies in the redshift range $1.5 < z < 3$ under the assumption that each galaxy once had or will undergo a quasar phase. We discuss the systematics involved and compare the results to mass-limited samples in the same redshift interval, extracted from the multi-wavelength surveys FIRES (Franx et al. 2000; Labbé et al. 2003; Förster Schreiber et al. 2006), GOODS-South (Giavalisco et al. 2004; Chapter 3), and MUSYC (Quadri et al. 2006).

We give an overview of the observations and simulations in §7.2 and §7.3 respectively. Next, the sample selection is explained in §7.4. §7.5 addresses the methodology to place the binary merger simulations in a cosmological context. We compare the predicted abundance of massive galaxies by the model to the observations in §7.6. The optical and optical-to-NIR color distribution of observed and simulated massive galaxies will be addressed in §7.7, followed by a discussion of their specific star formation rates (§7.8) and of the number and mass density of quiescent and star-forming massive galaxies in §7.9. We briefly compare observed and modeled pair statistics and address a few caveats on the observational and modeling results in §7.10. Finally, we summarize results in §7.11.

We work in the AB magnitude system throughout the chapter and adopt a $H0 = 70$ km s^{-1} Mpc^{-1}, $\Omega_M = 0.3$, $\Omega_\Lambda = 0.7$ cosmology.

7.2 Overview of the observations

7.2.1 Fields, coverage, and depth

We combine K_s-band selected catalogs of three different surveys: FIRES, GOODS-South, and MUSYC. The reduction and photometry of the FIRES observations of the Hubble Deep Field South (HDFS) is presented by Labbé et al. (2003) and was later augmented with IRAC data. The field reaches a K_s-band depth of 25.6 mag (AB, 5σ for point sources) and covers 5 arcmin^2. It was exposed in the WFPC2 U_{300}, B_{450}, V_{606}, I_{814} passbands, the ISAAC J_s, H, and K_s bands, and the 4 IRAC channels. Following similar procedures, a K_s-band selected catalog for the FIRES MS 1054–03 field was constructed by Förster Schreiber et al. (2006). The field, covering 24 arcmin^2, has a K_s-band depth of 25 mag (AB, 5σ for point sources). The catalog comprises FORS1 U, B, and V, WFPC2 V_{606}, and I_{814}, ISAAC J, H, and K_s, and IRAC 3.6 μm - 8.0 μm photometry.

Over a significantly larger area (113 arcmin^2), but to a shallower depth, a K_s-band selected catalog was constructed based on the publicly available GOODS-South data (Chapter 3). The variations in exposure time and observing conditions between the different ISAAC pointings lead to an inhomogeneous depth over the whole GOODS-South field. The 90% completeness level in the K_s-band mosaic is reached at an AB magnitude of $K_{s,AB}^{tot} = 23.7$. The photometry was performed in an identical way to that of the FIRES fields, allowing a straightforward combination of the three fields. The included passbands are the ACS B_{435}, V_{606}, i_{775}, and z_{850} bands, the ISAAC J, H, and K_s bands, and the 4 IRAC channels. We also use the ultradeep MIPS 24 μm (20 μJy, 5σ) imaging of the GOODS-South field. As for the IRAC bands, we used the information on position and extent of the sources from the higher resolution K_s-band image to reduce confusion effects on the 24 μm photometry (Labbé et al. in preparation).

Finally, we complement the FIRES and GOODS-South imaging with optical-to-NIR observations of the MUSYC HDFS1, HDFS2, and 1030 fields for parts of our analysis. The K_s-band selected catalogs are presented by Quadri et al. (2006). Together, the MUSYC fields span an area of 291 arcmin^2. They reach the 90% completeness level at $K_{tot,AB} = 22.7$. Given the current lack of IRAC data for the MUSYC fields and their shallower depth, they will only be used in the analysis of the rest-frame $U - V$ color distribution of the most massive ($M > 10^{11}$ $M_\odot$) high-redshift galaxies.

7.2.2 Redshifts and rest-frame photometry

Despite the large number of spectroscopic campaigns in the GOODS-South and FIRES fields, the fraction of K_s-selected $1.5 < z < 3$ galaxies that is spectroscopically confirmed is only 7%. The fraction drops to 3% when the MUSYC fields are included. Therefore, a reliable estimate of the photometric redshift is crucial in defining robust samples of massive high-redshift galaxies.

Förster Schreiber et al. (in preparation) used the algorithm developed by Rudnick et al. (2001, 2003) to fit a non-negative linear combination of galaxy templates to the optical-to-NIR spectral energy distribution of each galaxy. The template set used for the FIRES and GOODS-South fields consisted of 10 Single Stellar Population (SSP) templates with a Salpeter (1955) initial mass function and solar metallicity from the Bruzual & Charlot (2003, hereafter BC03) stellar population synthesis code, with ages logarithmically spaced between 50 Myr and 10 Gyr. Each of the templates was allowed to be attenuated according to the Calzetti et al. (2000) law by $E(B-V) = 0.0, 0.1, 0.3$, or 0.6.

The uncertainties in the photometric redshifts were determined from Monte Carlo simulations. For each galaxy, a set of 100 mock SEDs was created by perturbing each flux point according to its formal error bar, and repeating the z_{phot} computation. The lower and upper error on z_{phot} comprise the central 68% of the Monte Carlo distribution.

We tested the quality of the photometric redshifts in two ways. First we compare them to the available spectroscopic redshifts in the $1.5 < z < 3$ interval, resulting in a normalized median absolute deviation $\sigma_{NMAD}\left(\frac{z_{phot}-z_{spec}}{1+z_{spec}}\right) = 0.10$. The quality measure σ_{NMAD} remains the same when the spectroscopic redshifts in the MUSYC fields are included or excluded. Second we tested how well we could recover the redshift from synthetic broad-band photometry of simulated SPH galaxies placed at redshifts 1.5 to 3. We found that the considered template set performed very well [$\sigma_{NMAD}(\Delta z/(1+z)) = 0.03$]. The scatter in the comparison to spectroscopically confirmed galaxies is larger than that derived from the simulations. This is likely due to the fact that the synthetic photometry is based on the same stellar population synthesis code as the template set used to recover the redshifts. Therefore, the second test only studies the impact of an unknown star formation history, dust and metallicity distribution on the derived z_{phot}.

We computed the rest-frame photometry by interpolating between observed bands using the best-fit templates as a guide. Uncertainties in the rest-frame colors were derived from the same Monte Carlo simulations mentioned above, and comprise both a contribution from photometric uncertainties and from z_{phot} uncertainties. For a detailed description, we refer the reader to Rudnick et al. (2003).

7.2.3 Stellar masses

Förster Schreiber et al. (in preparation) derived stellar masses of the observed galaxies following the procedure described by Wuyts et al. (2007). Briefly, we fit BC03 templates to the optical-to-8 μm SED with the HYPERZ stellar population fitting code, version 1.1 (Bolzonella et al. 2000). We allow the following star formation histories: a single stellar population (SSP) without dust, a constant star formation history (CSF) with dust, and an exponentially declining star formation history with an *e*-folding timescale of 300 Myr (τ_{300}) with dust. The allowed A_V values ranged from 0 to 4 in step of 0.2, and the attenuation law applied was taken from Calzetti et al. (2000). We constrain the time since the onset of star formation to lie between 50 Myr and the age of the universe at the respective redshift. Finally, a Salpeter (1955) IMF was assumed with lower and upper mass cut-offs of 0.1 $M_\odot$ and 100 $M_\odot$. For consistency, the same IMF was adopted by the simulations.

7.2.4 Star formation rates

We derived estimates of the total (unobscured plus obscured) star formation rate of the observed galaxies by adding the UV and IR light, scaled by the calibrations for the local universe (Kennicutt 1998):

$$SFR\ [M_\odot\ \mathrm{yr}^{-1}] = 1.8 \times 10^{-10}\,(L_{IR} + 3.3L_{2800})\,/L_\odot \tag{7.1}$$

where the rest-frame luminosity $L_{2800} \equiv \nu L_\nu(2800\mathring{A})$ was derived from the observed photometry with the algorithm by Rudnick et al. (2003). The total IR luminosity $L_{IR} \equiv L(8 - 1000\ \mu\mathrm{m})$ was derived from the observed 24 μm flux density in combination with the photometric redshift estimate (spectroscopic when available) following the prescription of Dale & Helou (2002). As best estimate, we adopt the mean conversion factor of all Dale & Helou (2002) IR spectral energy distributions within the range $\alpha = 1 - 2.5$, where α parameterizes the heating intensity level from active ($\alpha = 1$) to quiescent ($\alpha = 2.5$) galaxies. The variation from $L_{IR,\alpha=2.5}$ to $L_{IR,\alpha=1}$ is 0.9 dex in the redshift interval $1.5 < z < 3$. Where relevant, we indicate this systematic uncertainty in the conversion from 24 μm to L_{IR} and eventually star formation rate in the plots.

7.3 Overview of the simulations

We use a set of smoothed particle hydrodynamics (SPH, Lucy 1977; Gingold & Monaghan 1977) simulations performed by Robertson et al. (2006) of co-planar, equal-mass, gas-rich ($f_{gas} = 0.8$) mergers over a range of galaxy masses. A description of the GADGET-2 code used to run the simulations is given by Springel (2005b). Springel & Hernquist (2003) describe the prescriptions for star formation and supernova feedback. The interplay between the supermassive black hole(s) and the environment is discussed by Springel et al. (2005b). We refer the reader to Robertson et al. (2006) for specifications on this particular set of simulations and an explanation of how the progenitors were scaled to approximate the structure of disk galaxies at redshift $z = 3$. The photometry of the snapshots was derived in post-processing as described in Chapter 6.

Briefly, the total attenuated spectral energy distribution (SED) for a given snapshot consisting of N stellar particles is computed as follows:

$$\begin{aligned} L_{Att,tot}(\lambda) &= \sum_{i=1}^{N} \ m_i \cdot L_{Int}(age_i, Z_i, \lambda) \\ &\qquad \cdot \exp\left[-NH_{i,los} \cdot \frac{Z_{i,los}}{Z_\odot} \cdot \sigma(\lambda)\right] \end{aligned} \tag{7.2}$$

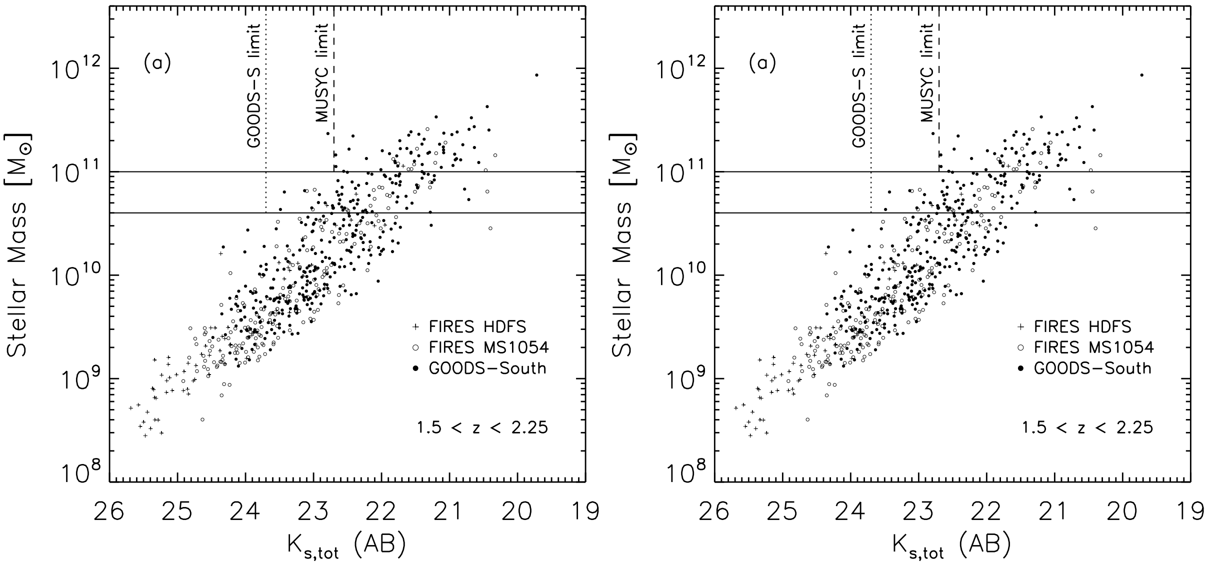

Figure 7.1 — The relation between stellar mass and observed total K_s magnitude for galaxies in the FIRES and GOODS-South fields at (a) $1.5 < z < 2.25$ and (b) $2.25 < z < 3$. The solid lines show the adopted $\log M > 10.6$ (FIRES+GOODS-South) and $\log M > 11$ (FIRES+GOODS-South+MUSYC) mass limits. The dotted line indicates the photometric limit of the GOODS-South imaging. The dashed line indicates the approximate limit for the MUSYC fields. There are few galaxies with $\log M > 10.6$ and $K_{s,tot} > 23.7$, or $\log M > 11$ and $K_{s,tot} > 22.7$. The largest incompleteness correction is needed for the highest redshift bin in the MUSYC fields. A third of the $\log M > 11$ galaxies would be undetected by MUSYC, as estimated from the deeper FIRES+GOODS fields.

where m_i, age_i, and Z_i are, respectively, the mass, age, and metallicity of stellar particle i that is treated as a single stellar population. L_{Int} is the intrinsic (unattenuated) SED interpolated from a grid of templates from a stellar population synthesis code. Here, we use SSP templates from BC03 as default. Results obtained when using a grid of Maraston (2005, hereafter M05) SSP templates for different ages and metallicities will be addressed as well. Parameters in Eq. 7.2 that are dependent on the line of sight are subscripted with "los". To each stellar particle, the column density of hydrogen and the average metallicity along the line of sight was computed for 100 viewing angles, uniformly spaced on a sphere. The optical depth is proportional to this metallicity-scaled column density, with the wavelength dependence adopted from an attenuation law (parameterized by the cross section $\sigma(\lambda)$). We use the Calzetti et al. (2000) reddening curve unless mentioned otherwise. The change in predicted colors when adopting the SMC-like attenuation law from Pei (1992) will be discussed as well.

7.4 Sample selection

Our aim is to compare the color distribution, number and mass density of mass-limited samples of observed and simulated galaxies. We choose the mass-limit such that the observed sample is reasonably complete in the considered redshift interval, even for the field with the shallowest K_s-band depth from which the sample was drawn. In order to optimally exploit the range in area and depth of the considered surveys, we define two mass-limited samples and divide each in two redshift bins: $1.5 < z < 2.25$

and $2.25 < z < 3$, probing a similar comoving volume. The first sample contains galaxies more massive than $\log M = 10.6$ ($M \simeq 4 \times 10^{10}\ M_\odot$) in the FIRES and GOODS-South fields. It contains 152 and 84 objects in the low- and high-redshift bin respectively. We present the sample in Figure 7.1, where we plot the stellar mass of all FIRES and GOODS-South sources that are detected above the 5σ level in the respective redshift bin against their total observed K_s-band magnitude. The stellar mass correlates with the K_s-band magnitude, but a scatter of an order of magnitude is present due to the range in redshifts and spectral types of the galaxies. The 90% completeness limit ($K_{s,tot} = 23.7$) for the GOODS-South field , which is shallower than the FIRES fields, is indicated with the dotted line. At $1.5 < z < 2.25$, no massive ($\log M > 10.6$) galaxies fainter than $K_{s,tot} = 23.7$ are found in the FIRES fields and deeper parts of the GOODS-South mosaic. The lowest K_s-band signal-to-noise ratio in the massive galaxy sample is $S/N_{K_s} \simeq 12$, strongly suggesting that no incompleteness correction is needed to compute the number and mass density in the $1.5 < z < 2.25$ redshift bin. In the $2.25 < z < 3$ redshift bin, we find four well-detected massive ($\log M > 10.6$) galaxies fainter than the 90% completeness limit of GOODS-South. Three out of 4 have $6.4 < S/N_{K_s} < 10$, whereas all other massive galaxies are detected above the 10σ level. Evaluating the fraction of massive galaxies fainter than $K_{s,tot} = 23.7$ in the area that is sufficiently deep to detect these sources, we estimate the completeness in the high-redshift bin to be $\sim 95\%$.

In order to reduce the uncertainty from cosmic variance in the derived number and mass densities, we also compose a sample including the MUSYC fields, increasing the sampled area by roughly a factor of 3. The shallower depth forces us to restrict the mass limit to $M > 10^{11}\ M_\odot$. We derive the completeness in the two redshift intervals using the deeper FIRES and GOODS-South fields in Figure 7.1. The dashed line marks the approximate depth (90% completeness) for the MUSYC fields. 1.5% of the $1.5 < z < 2.25$ galaxies with $\log M > 11$ in the deeper FIRES and GOODS-South fields are fainter than this limit. For the $2.25 < z < 3$ bin, the fraction of massive galaxies that would be missed by MUSYC increases to 33%. In our analysis, we will mention both the directly measured number and mass densities and those obtained after the incompleteness correction.

7.5 Methodology for cosmological context

To date, hydrodynamical simulations including a self-consistent treatment of SMBH growth have only been run with adequate resolution on binary merger systems (Springel et al. 2005a; Di Matteo et al. 2005; Robertson et al. 2006; Cox et al. 2006) or as zoom-in on overdense regions of cosmological N-body simulations at very high redshift $z \sim 6$ (Li et al. 2006). In order to confront observations of $1.5 < z < 3$ galaxies with the hydrodynamical simulations, we place the binary mergers in a cosmological context using the observed quasar luminosity function following the prescription by Hopkins et al. (2006b).

Briefly, the conversion from quasar demographics to galaxy demographics goes as follows. From a large set of binary merger simulations, Hopkins et al. (2006a) determined the distribution of quasar lifetimes, describing the time $\frac{dt(L,L_{peak})}{d\log(L)}$ spent by a

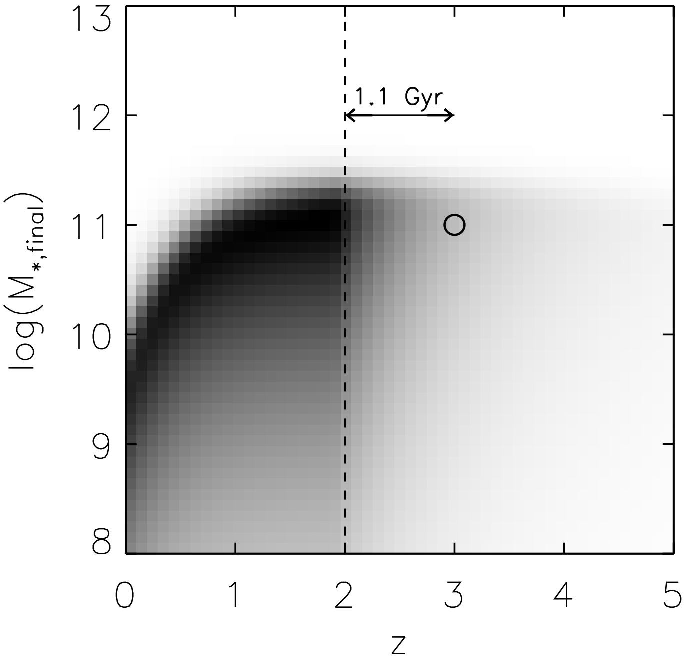

Figure 7.2 — The birth rate of spheroids (in greyscale) as a function of redshift and final stellar mass as derived from the observed quasar luminosity function. The meaning of the time scale arrow and the open circle is described in the text. The model by Hopkins et al. (2006b) assumes that this birth rate equals the merger rate of galaxies. The birth rate (i.e., merger rate) reaches a maximum of 4.5×10^{-4} $\log M^{-1}$ Mpc^{-3} Gyr^{-1} at $z \sim 2$. As time evolves, the peak of the merger rate function shifts toward lower mass galaxies.

quasar of peak luminosity L_{peak} in the luminosity interval $d\log(L)$. The observed quasar luminosity function simply corresponds to the convolution of this differential quasar lifetime with the birth rate $\dot{n}(L_{peak})$ of quasars with peak luminosity L_{peak}:

$$\Phi(L) = \int \frac{dt(L, L_{peak})}{d\log(L)} \, \dot{n}(L_{peak}) \, d\log L_{peak} \tag{7.3}$$

Using a compilation of observed quasar luminosity functions in the hard X-rays (Ueda et al. 2003), soft X-rays (Hasinger, Miyaji,& Schmidt 2005), and optical (Richards et al. 2005), Eq. 7.3 was then de-convolved to solve for $\dot{n}(L_{peak})$. The relation between peak luminosity of the quasar and the final black hole mass, derived from the same simulations, was then adopted to calculate the birth rate of black holes of a certain final mass $\dot{n}(M_{BH})$. This function was on its turn converted to a birth rate of spheroids $\dot{n}(M_{sph})$ as a function of their final stellar mass using the SMBH-host connection $M_{BH} = 0.0012 \frac{(1+z^{2.5})}{\left(1+\left(\frac{z}{1.775}\right)^{2.5}\right)} M_{sph}$ (Hopkins et al. 2007).

The model by Hopkins et al. (2006b) assumes that the birth rate of spheroids equals the major merger rate of galaxies. The resulting merger rate as a function of stellar mass is displayed with greyscales in Figure 7.2 (darker meaning a higher merger rate). Its redshift dependence was derived by considering observed quasar luminosity functions at a range of redshifts. The peak of the merger rate at $z \sim 2$ has a value of 4.5×10^{-4} $\log M^{-1}$ Mpc^{-3} Gyr^{-1}. A clear trend is visible of mergers occuring in lower mass systems as we proceed in time (i.e., to lower redshifts) after this peak. If mergers are responsible for a significant part of the growth in stellar mass, this trend explains at least qualitatively the observed downsizing of star formation over cosmic time (Cowie et al. 1996).

To evaluate the post-merger (i.e., post-quasar, since the merging event triggers

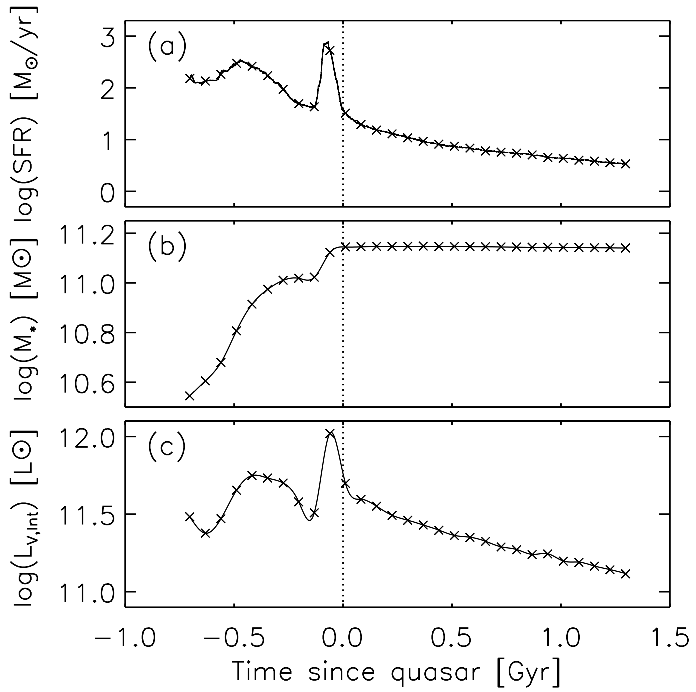

Figure 7.3 — Typical evolution of a merger simulation: (a) star formation history, (b) history of the mass build-up, and (c) evolution of the rest-frame *V*-band luminosity. The dotted line indicates when the peak in quasar luminosity is reached. For a detailed description of the time evolution in these and other parameters (e.g., accretion rate, quasar luminosity, extinction) we refer the reader to Hopkins et al. (2006a) and Chapter 6.

quasar activity in the simulations) galaxy population at $z \sim 2$, we integrate the merger rate function from $z = \infty$ to 2 and over the whole stellar mass range. For example, when the integration reaches ($M_{*,final} = 10^{11}\ M_{\odot}$; $z = 3$), marked by the circle in Figure 7.2, we compute the photometry of a merger simulation with a final stellar mass of $10^{11}\ M_{\odot}$ at 1.1 Gyr after the peak of quasar luminosity (the time elapsed between $z = 3$ and $z = 2$). As explained in §7.3, we compute the synthetic photometry along 100 lines of sight, uniformly spaced on a sphere. The number density of galaxies at $z = 2$ with colors corresponding to the 100 lines of sight is then scaled according to the value of the merger rate function at ($M_{*,final} = 10^{11}\ M_{\odot}$; $z = 3$). Finally, a mass cut is applied to guarantee an identical selection of observed and simulated galaxies.

In order to predict the abundance and properties of galaxies at $z \sim 2$ that have yet to reach their peak in quasar luminosity or did not even start merging at the evaluated epoch, one can in principle integrate the merger rate function down to lower and lower redshifts. How far one integrates beyond the evaluated redshift is a rather arbitrary choice. We caution that counting galaxies long before they will contribute to the quasar luminosity function will lead to large uncertainties given their unconstrained pre-merger history. The typical evolution of a merger simulation is illustrated in Figure 7.3 where we plot the star formation rate, stellar mass, and rest-frame *V*-band luminosity as a function of time since the peak in quasar luminosity. We decide to integrate 700 Myr beyond the evaluated redshift, thus counting both the galaxies that are undergoing a merger-induced nuclear starburst (sometime between 0 and 200 Myr before the quasar phase) and those with star formation triggered by the first passage (sometime between 200 and 700 Myr before the quasar phase). Hereafter, we will refer to all galaxies in an evolutionary stage between 0 and 700 Myr before the quasar phase as merging galaxies. Such a prediction only counts those galaxies that will later merge and produce a quasar. Apart from predicting the abundance and properties of

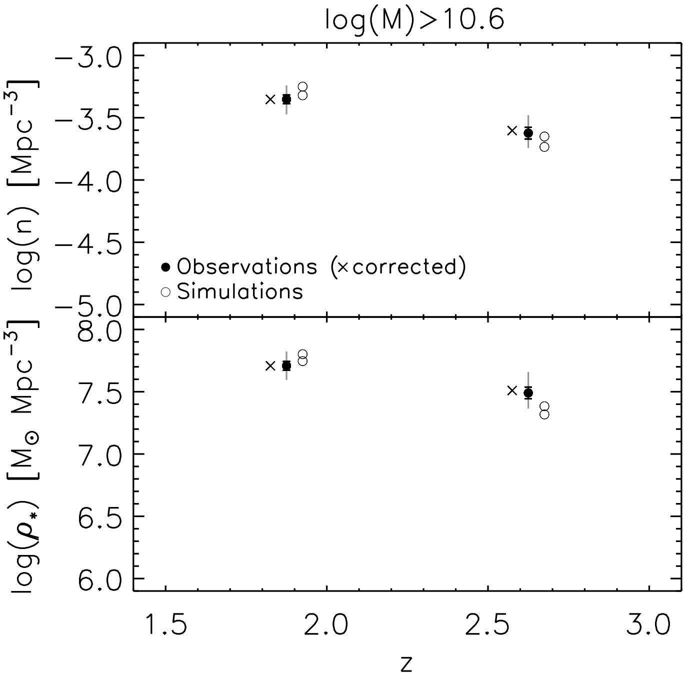

Figure 7.4 — The number and mass density of observed (*filled symbols*; FIRES + GOODS-S) and modeled (*empty symbols*) galaxies with $\log M > 10.6$ as a function of redshift. The cross symbols indicate the observed number and mass density after a correction for incompleteness. The black error bar represents the Poisson shot noise solely. The grey error bar accounts for uncertainties in redshift and mass, and a (dominating) contribution from cosmic variance. We find that both the predicted number and mass densities agree within the error bars with the observed values.

the post-quasar population, we will thus be able to constrain how much of the massive star-forming galaxies can be accounted for by merger-induced star formation.

Provided the assumption of a one-to-one correspondence between quasars and major mergers is valid, the formal uncertainty in the merger rate function presented in Figure 7.2 originates mostly from the weakly constrained faint end of the observed quasar luminosity function, where one can assume a pure luminosity evolution or also a slope evolution. At the bright end, and therefore for our massive galaxy samples, the predictions are robust, as will be indicated in due time.

7.6 The number density, mass density and mass function of galaxies with $\log \mathbf{M} > 10.6$ at $1.5 < z < 3$

Before analyzing the observed and modeled massive galaxy sample as a function of color and galaxy type, we consider the overall abundance of galaxies above $\log M > 10.6$. We computed the model number and mass density by integrating the merger rate function to 700 Myr beyond the evaluated redshift, i.e., including galaxies up to 700 Myr before the quasar phase. The number and mass densities of galaxies with $\log M > 10.6$ predicted by the model (*empty symbols*) are compared against the abundance of observed galaxies (*filled symbols*) above the same mass limit in Figure 7.4. The results are listed in Table 7.1. The spread of the empty circles indicates the freedom allowed by the model due to the weakly constrained faint end of the quasar luminosity function.

The cross symbols represent the observed number and mass density after applying a 0% and 5% correction for incompleteness in the low- and high-redshift bin respectively. We considered three sources of error in the observations: Poisson shot noise, cosmic variance and selection uncertainties stemming from uncertainties in the redshift and the mass of individual galaxies. The black error bars in Figure 7.4 indicate the contribution from Poisson noise, ranging from 8 to 10%. We are more severely limited by cosmic variance. We follow the method outlined by Somerville et al. (2004) to calculate the cosmic variance as predicted from cold dark matter theory for a population with unknown clustering as a function of its number density and the probed comoving volume of the sample. The resulting contribution to the error budget is 28% for the $1.5 < z < 2.25$ and 29% for the $2.25 < z < 3$ redshift bin. Finally, the uncertainties in the individual redshift and mass determinations propagate into the number and mass density of quiescent red galaxies. We estimate the contribution to the total error budget from Monte Carlo simulations. We constructed 1000 mock catalogs for the FIRES and GOODS-South fields by perturbing the redshift, rest-frame colors, and stellar masses so that 68% of the perturbed values lie within the formal 1σ lower and upper limits. The uncertainties in the photometric redshift and the rest-frame colors were derived as explained in §7.2.2. For the mass estimates, we adopt a lower error bar of -0.1 dex and upper error bar of +0.04 dex for all merger remnants. This corresponds to the quality with which stellar masses were recovered from synthetic photometry of simulated merger remnants when applying the same SED modeling procedure as we use for our observations (Chapter 6). The median recovered mass was only 0.01 dex lower than the true stellar mass of the simulated merger remnants, suggesting that systematic offsets are negligible for this type of galaxies. For star-forming galaxies that have yet to reach their quasar phase we found a typical mass underestimate of -0.1 dex, with the central 68% interval of $\Delta \log M \equiv \log M_{recovered} - \log M_{true}$ ranging from -0.25 to 0 dex. We should keep in mind however that the input photometry for this test and the templates used to recover the masses are based on the same stellar population synthesis code. It has been noted by several authors (Maraston et al. 2006; van der Wel et al. 2006; Wuyts et al. 2007) that the use of M05 templates instead of BC03 templates leads to stellar mass estimates that are lower by a factor 1.5.

After constructing the 1000 mock catalogs, we apply the same sample selection (redshift interval, $\log M > 10.6$) and compute the number and mass density for each of them. The lower and upper limits comprising 68% of the distribution of mock number and mass densities were added in quadrature to the uncertainty from Poisson shot noise and cosmic variance, shown with the grey error bar in Figure 7.4. The uncertainty in the number density propagating from redshift and mass uncertainties for individual objects amounts to 5% and 10% for the low- and high-redshift bin. The contribution to the uncertainty in the mass density is 6% and 14% for the low- and high-redshift bin respectively. We conclude that, even with the 142 arcmin^2 area of our combined deep fields, cosmic variance is still the limiting factor for the determination of the number and mass density of quiescent red galaxies.

Figure 7.4 shows that the model number and mass density for the population of massive ($\log M > 10.6$) galaxies as a whole agrees within the error bars with the observations. Plotting the mass function for the observations (*black histogram*) and the model (*dark-grey polygon*) in Figure 7.5, we find that the comparable abundance of observed and modeled galaxies still holds when studied as a function of galaxy mass. With lighter grey polygons, we illustrate the model prediction when including only galaxies up to 200 Myr before the merger ($t >$ -200 Myr) or only merger remnants ($t > t_{QSO}$). The width of the polygons reflects the uncertainty in the merger rate func-

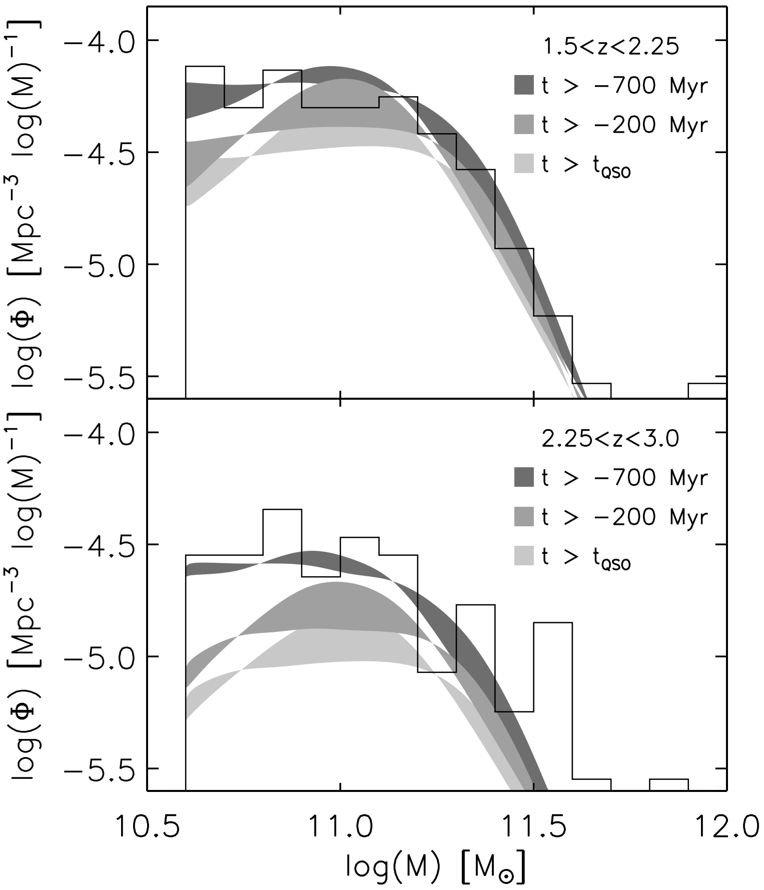

Figure 7.5 — The mass function of observed (*black histogram*; FIRES + GOODS-S) and modeled (*grey polygons*) galaxies with $\log M > 10.6$ at redshift $1.5 < z < 2.25$ (*top panel*) and $2.25 < z < 3.0$ (*bottom panel*). Merger remnants alone ($t > t_{QSO}$) cannot account for the total population of observed galaxies above the same mass limit. Integrating the merger rate function to include galaxies up to 700 Myr before the quasar phase results in a mass function that is consistent with the observations.

tion. We conclude that merger remnants alone cannot account for the entire observed massive galaxy population. However, including galaxies with merger-triggered star formation, the mass function predicted by the model is in good agreement with the observations. This results strengthens the idea that the model fairly reflects reality and encourages a more detailed investigation of the properties of observed and simulated massive galaxies.

7.7 The color distribution of galaxies with $\log \mathbf{M} > 10.6$ at $1.5 < z < 3$

7.7.1 The U − V color distribution

First, we consider the optical color distribution of our sample of FIRES and GOODS-South galaxies with $M > 4 \times 10^{10}\ M_{\odot}$. A histogram of their rest-frame $U - V$ colors is plotted with a solid line in Figure 7.6(a) and Figure 7.6(b) for the low- and high-redshift bin respectively. No corrections for incompleteness were applied here, but we remind the reader that those are negligible for the low-redshift bin and of the order of 5% only for the high-redshift bin. The total number of massive galaxies is 152 and 85 in the low- and high-redshift bin respectively. They span a broad $U - V$ color range. In both cases, the median color is $U - V = 1.5$ and 68% of the galaxies in each redshift bin lie within the $1.1 < U - V < 1.9$ interval.

It is interesting to consider whether the descendants and progenitors of quasars (or rather quasar hosts) above the same mass limit show colors that are similar and

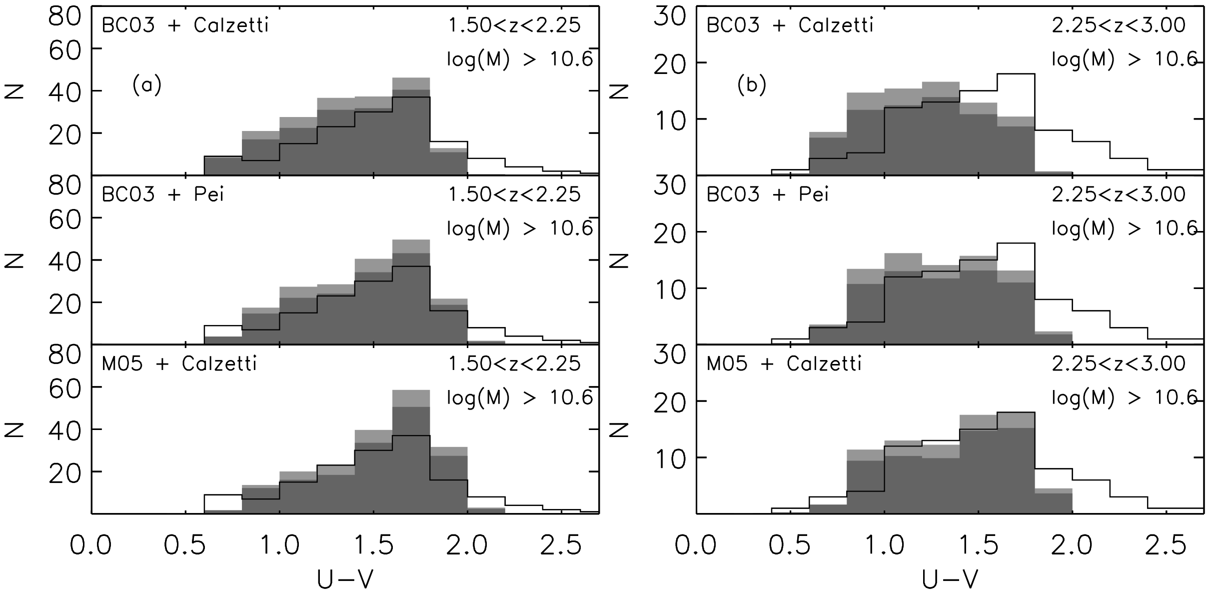

Figure 7.6 — The rest-frame $U - V$ color distribution of observed galaxies with masses above $\log M = 10.6$ in the FIRES and GOODS-South fields (*solid line*) for the redshift intervals (a) $1.5 < z < 2.25$ and (b) $2.25 < z < 3$. With filled histograms, we overplot the predicted $U - V$ color distribution of merging and post-quasar galaxies, scaled to the same solid angle as the observations. The light-grey top of the model histogram indicates the uncertainty in the merger rate function used to place the simulated mergers in a cosmological context. For a given redshift interval, the model predictions in the three panels give an indication of the uncertainty in the synthetic photometry induced by the choice of attenuation law (Calzetti et al. 2000 versus the SMC curve from Pei 1992) and the choice of stellar population synthesis code (BC03 versus M05). Overall, the predicted color distribution coincides with that of the observed massive galaxy sample, with roughly equal numbers. The model distribution in the high-redshift bin (b) shows a slight excess at blue $U - V$ colors. The red tail of the observed color distribution is not reproduced by the modeled merger and post-quasar population.

come in numbers comparable to those of the observed massive galaxy sample. In this section, we focus mainly on the first question, but note in passing that we show the predicted color distribution scaled to the same solid angle as probed by the FIRES and GOODS-South observations. The filled grey histograms show the synthetic photometry of merger simulations in either their post-quasar phase or in a phase of at most 700 Myr before their peak in quasar luminosity. The numbers at each color are derived from the observed quasar luminosity function by integrating the merger rate function from $z = \infty$ to 700 Myr beyond the evaluated redshift as described in §7.5. The colors of different evolutionary phases will be discussed separately in due time. The difference between the dark- and light-grey histogram reflects the uncertainty in the merger rate function, itself due to uncertainties in the observed quasar luminosity function. Apart from uncertainties in the merger rate function, uncertainties in the synthetic photometry for a given simulation snapshot contribute to the total error budget of the model predictions. To translate the simulated properties such as age, mass, and metallicity of the stellar particles to observables, we make use of a stellar population synthesis code to compute the intrinsic colors and assume an attenuation law to calculate the dimming and reddening by dust. We investigate the dependence on attenuation law empirically by computing the synthetic photometry using a Calzetti et al. (2000) reddening curve and the SMC-like reddening curve from Pei (1992). We note that the synthetic colors derived with the Milky Way-like attenuation curve by Pei (1992) lie in between those produced by the two reddening curves considerd here. This is demonstrated in Chapter 6. Similarly, we test the dependence on adopted stellar population synthesis templates empirically by computing the synthetic photometry based on a grid of BC03 single stellar populations (SSPs) and based on a grid of SSPs by M05.

We note that the choice of attenuation law has a minor effect only on the $U-V$ color. The use of M05 templates gives the simulated galaxies a slightly redder color. Overall, the same conclusion can be drawn independent of the way the model color distribution was computed. Namely, the simulated galaxies with $\log M > 10.6$ span a color range that reaches from the bluest observed $U-V$ colors to $U-V \sim 2$. At $1.5 < z < 2.25$, the color distribution resembles remarkably well that of the bulk of the observed massive galaxies, both in shape and numbers. At $2.25 < z < 3$, the predicted model colors show a slight excess at blue $U-V$ colors. In both redshift bins, the modeled color distribution does not reach the reddest $U-V$ colors of observed galaxies above the same mass limit. The good overall correspondence between the observed and modeled optical color distributions gives a first indication that the number of massive post-quasar galaxies plus the number of galaxies in the process of merging at $1.5 < z < 3$ as expected from the observed quasar luminosity function may account for a large fraction of the observed massive galaxy population at $1.5 < z < 3$.

7.7.2 The $\mathbf{V-J}$ color distribution

Turning to longer wavelengths, we now compare the $V-J$ colors predicted for mergers and merger remnants (i.e., post-quasars) with masses above $\log M = 10.6$ to the color distribution of observed galaxies in the same redshift interval and above the same mass limit (Figure 7.7).

Again, the color distribution of our observed massive galaxy sample has a large range of colors, reaching from $V-J = 0.5$ to $V-J = 2.5$ and peaking centrally at $V-J = 1.3$ and 1.2 for the low- and high-redshift bin respectively. The central 68% interval is $1.0 < V-J < 1.8$ and $0.8 < V-J < 1.8$ for the low- and high-redshift bin respectively.

As for the $U-V$ color distribution, we find that the adopted attenuation law has only a minor influence on the color distribution, reaching at most shifts of 0.2 mag toward redder $V-J$ colors when the SMC-like reddening curve from Pei (1992) is used instead of the Calzetti et al. (2000) attenuation law. Comparing the model $V-J$ color distribution derived from BC03 or M05 templates immediately shows that the predictive power of the merger model is strongly hampered by the uncertainties in the rest-frame NIR wavelength regime that today's stellar population synthesis codes are facing. In the low- and high-redshift bin, the median $V-J$ color of the model distribution is 0.4 and 0.5 mag redder when using M05 than when using BC03. One of the main differences between the BC03 and M05 templates is the treatment of thermally pulsating AGB stars. Using the fuel consumption approach as M05 does instead of the isochrone synthesis approach that BC03 follow, one finds significantly larger NIR luminosities for SSPs at ages between 0.2 and 2 Gyr. For an in-depth discussion of

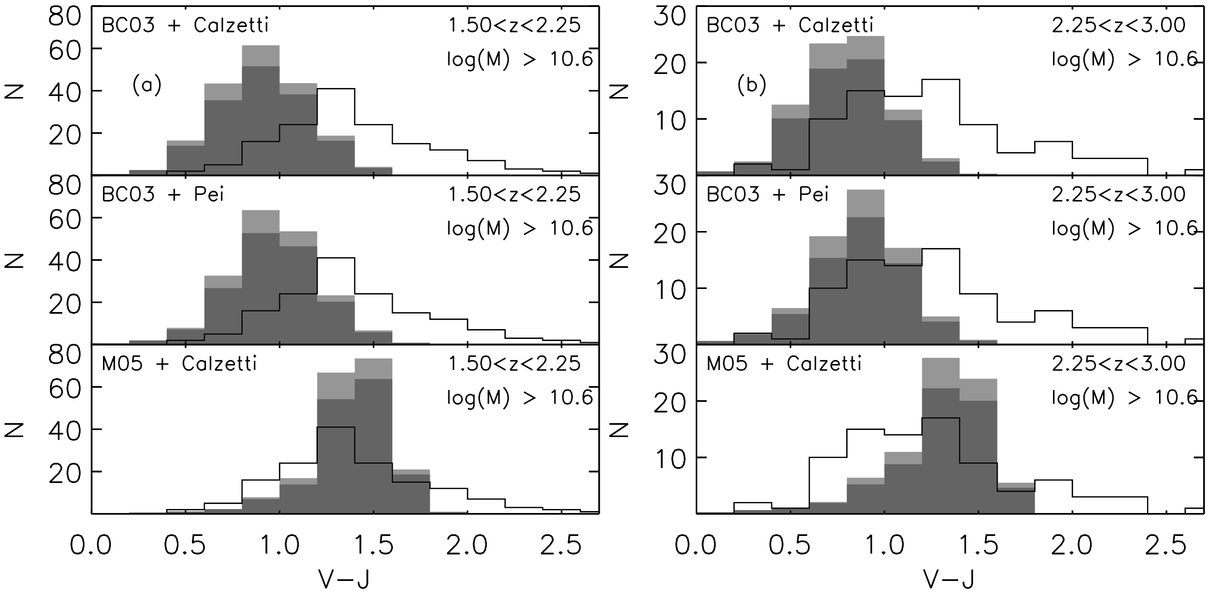

Figure 7.7 — The rest-frame $V - J$ color distribution of observed galaxies with masses above $\log M = 10.6$ in the FIRES and GOODS-South fields (*solid line*) for the redshift intervals (a) $1.5 < z < 2.25$ and (b) $2.25 < z < 3$. With filled histograms, we overplot the predicted $V - J$ color distribution of merging and post-quasar galaxies, scaled to the same solid angle as the observations. The light-grey top of the model histogram indicates the uncertainty in the merger rate function used to place the simulated mergers in a cosmological context. For a given redshift interval, the model predictions in the three panels give an indication of the uncertainty in the synthetic photometry induced by the choice of attenuation law (Calzetti et al. 2000 versus the SMC curve from Pei 1992) and the choice of stellar population synthesis code (BC03 versus M05). The model $V - J$ color distribution is weakly constrained by the uncertainties at NIR wavelengths in the stellar population synthesis codes. Nevertheless, we can conclude that there exist massive galaxies with redder $V - J$ colors than those of modeled merging and post-quasar galaxies.

the differences between the two codes, we refer the reader to Maraston (2005) and Maraston et al. (2006). It is worth stressing that, irrespective of whether the BC03 or M05 stellar population synthesis code is used, the red ($V - J > 1.8$) tail of the observed distribution has no counterparts in the modeled color distribution of merging and post-merger galaxies. Conversely, an excess of galaxies is found at blue ($V - J \sim 0.9$) or intermediate ($V - J \sim 1.4$) optical-to-NIR colors for the BC03 and M05 model color distributions respectively.

7.7.3 U − V versus V − J color-color distribution

7.7.3.1 *Quiescent red galaxies*

Recently, a diagnostic color-color diagram of observer-frame $I - K$ versus K-[4.5 μm] has been proposed by Labbé et al. (2005) to distinguish three basic types of $z > 2$ galaxies. The rest-frame equivalent of this diagram, $U - V$ versus $V - J$, was presented by Wuyts et al. (2007), allowing a comparison of galaxies over a wider redshift range. First, there are galaxies with relatively unobscured star formation, such as Lyman break galaxies (Steidel et al. 2003) and their lower redshift BX/BM analogs (Adelberger et al. 2004). Their young ages and low reddening values result in blue colors, both in the

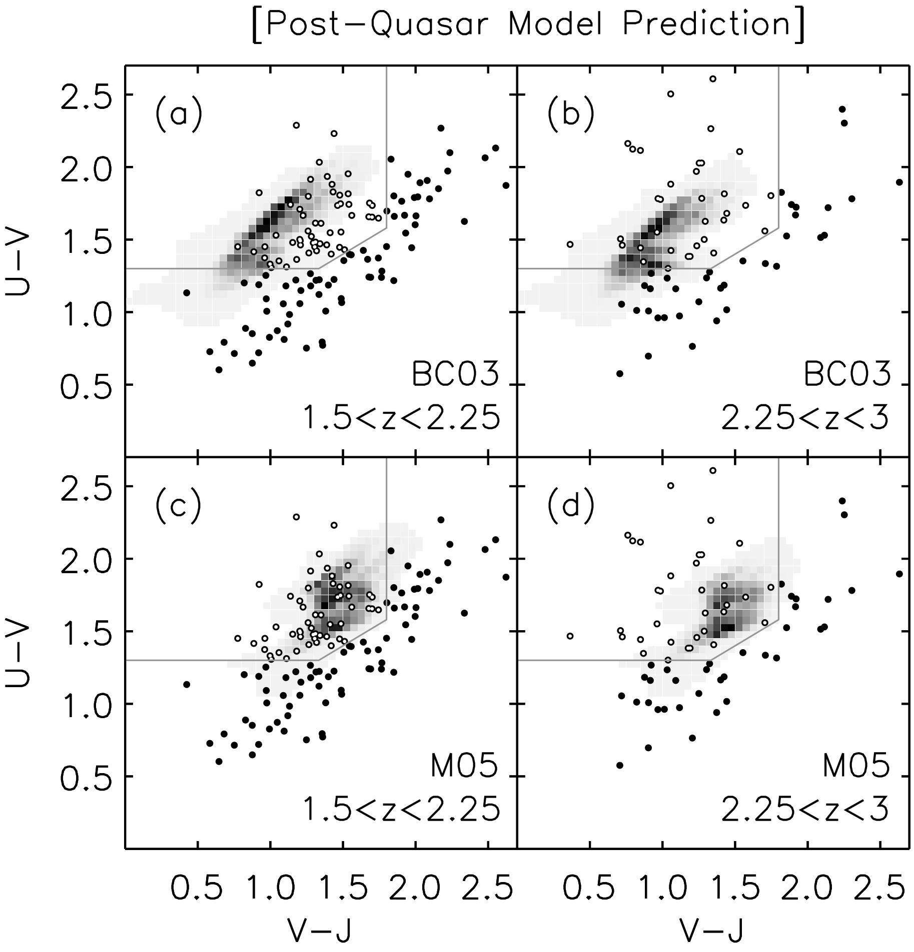

Figure 7.8 — Model $U-V$ versus $V-J$ color-color distribution of simulated galaxies with $\log M > 10.6$ that have had a merger and quasar phase in their past (*greyscales*), with a darker intensity indicating a larger number of post-quasars. Observed galaxies above the same mass limit in the FIRES and GOODS-South fields are overplotted. Empty symbols mark the galaxies that satisfy the quiescent galaxy criterion, whose selection window is marked by the grey wedge. A notable difference between the synthetic photometry derived using the BC03 and M05 stellar population synthesis code is the redder $V-J$ color in the latter case. Recognizing this uncertainty in the model prediction, we can still conclude that the predicted color distribution of post-quasars roughly coincides with that of quiescent red galaxies.

rest-frame optical and in the rest-frame optical-to-NIR. Second, there is a population of star-forming galaxies with much redder colors, due to the presence of dust. Their intrinsic (unobscured) colors are similar to those of Lyman break galaxies, but they are driven along the dust vector toward redder $U-V$ and redder $V-J$ colors. Finally, a population of galaxies with red $U-V$ colors is present at $z \sim 2$ whose SED is well matched by that of a passive or quiescently star-forming galaxy at an older age. Their $V-J$ colors are relatively blue compared to those of dusty starbursts at the same optical color.

Labbé et al. (in preparation) designed a color criterion to select the quiescent red galaxies based on their rest-frame U, V, and J photometry. The selection window is defined as follows:

$$U - V > 1.3 \;\&\; V - J < 1.8 \;\&\; U - V > 0.6(V - J) + 0.5 \tag{7.4}$$

The validity of this selection criterion was confirmed by the fact that quiescent $z \sim 2$ galaxies with a prominent Balmer/4000Å break in their rest-frame optical spectra mostly lie within the wedge. Conversely, MIPS detected galaxies at $z \sim 2$, suggesting dust-enshrouded star formation, tend to lie redward of the wedge. We draw the wedge in Figure 7.8 and indicate the location of all galaxies with $\log M > 10.6$ in the FIRES and GOODS-South fields in the color-color diagram. Empty circles mark the objects that satisfy Eq. 7.4.

We also present a binned representation of the model color-color distribution of post-quasar galaxies only in Figure 7.8. The panels correspond to the $1.5 < z < 2.25$ and $2.25 < z < 3$ redshift bins, and model photometry derived from BC03 and M05 templates respectively. The color-color distribution computed with the SMC-like reddening curve from Pei (1992) instead of the Calzetti et al. (2000) law is not plotted, but looks very similar.

We conclude that in all realizations of the synthetic photometry, the predicted color-color distribution of the post-quasar population coincides more or less with the region of color-color space selected by the quiescent galaxy criterion.

7.7.3.2 Star-forming galaxies

A significant fraction ($\sim 50\%$) of the observed massive galaxy population at $1.5 < z < 3$ has colors located outside the quiescent red galaxy wedge. These objects reach from blue $U - V$ colors typical for Lyman break galaxies, which are known to host relatively unobscured star formation, up to the redder optical and optical-to-NIR colors from galaxies that are believed to host heavily obscured star formation. Here, we investigate whether the predicted color-color distribution for merging galaxies that will undergo a quasar phase in less than 700 Myr can reproduce the color range of observed star-forming galaxies. Figure 7.9 compares the model prediction (*greyscales*) to the observed massive galaxy colors (*empty circles* for star-forming galaxies).

As could be anticipated from §7.7.2, the model photometry does not reproduce the colors of observed dusty star-forming galaxies ($U - V > 1.3$ and outside the quiescent red galaxy wedge).

At bluer $U - V$, the synthetic photometry based on M05 templates gives a decent match to the observations, whereas the BC03 colors in combination with a Calzetti et al. (2000) attenuation law are offset by a few 0.1 mag toward bluer $V - J$.

7.8 Specific star formation rate as a function of stellar mass

So far, we have compared the synthetic colors of merging and post-quasar galaxies with those of observed star-forming and quiescent galaxies respectively. The separation between star-forming and quiescent galaxies for our observed galaxies was based on their broad-band optical-to-NIR colors. As an independent check, we now use the UV + 24 μm derived star formation rates to compare the observed distribution of specific star formation rates as a function stellar mass with the distribution predicted by

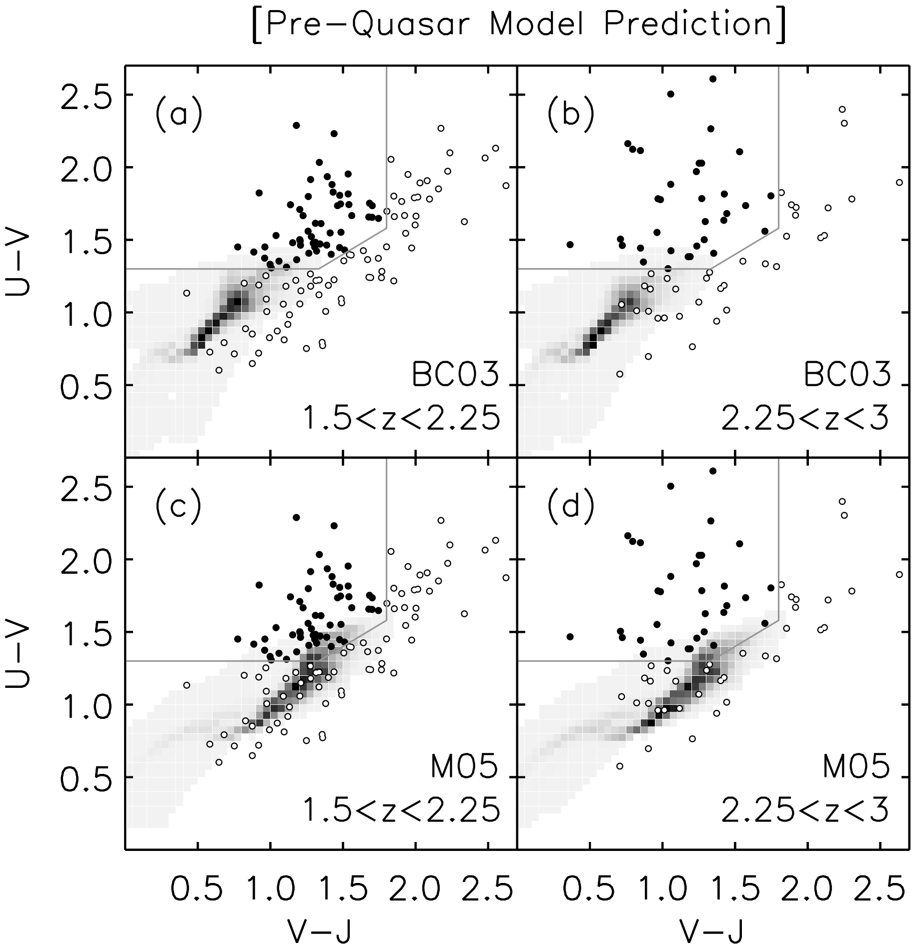

Figure 7.9 — Model $U - V$ versus $V - J$ color-color distribution of simulated galaxies with $\log M > 10.6$ that will undergo a quasar phase in less than 700 Myr (*greyscales*), with a darker intensity indicating a larger number of galaxies. Observed galaxies above the same mass limit in the FIRES and GOODS-South fields are overplotted. Empty symbols mark the galaxies that fall outside the quiescent galaxy criterion (*grey wedge*). A notable difference between the synthetic photometry derived using the BC03 and M05 stellar population synthesis code is the redder $V - J$ color in the latter case. (a) and (b) The model colors based on BC03 are a poor match to the observed star-forming galaxies (*empty symbols*). The $V - J$ colors fall blueward of the observed distribution, and only the lower half of the observed $U - V$ distribution of star-forming galaxies is reproduced. (c) and (d) The model colors based on M05 give a better match in the blue $U - V$ regime, but objects with $V - J \gtrsim 2$ are missing.

the merger model. The specific star formation rate is defined as the ratio of the star formation rate over the stellar mass. It equals the inverse of a mass-doubling time in the case of constant star formation. Here, we limit our sample to the GOODS-South field, where the 24 μm imaging is sufficiently deep (20 μJy, 5σ) to obtain useful constraints on the star formation rates.

Figure 7.10 shows the binned model distribution in greyscales and overplotted are the observed massive galaxies that fall inside (*empty symbols*) and outside (*filled symbols*) the quiescent red galaxy wedge. Upper limits are drawn for objects that were undetected by MIPS. Cross symbols mark those objects that are detected in the 1 Ms Chandra X-ray exposure (Giacconi et al. 2001). We caution that the 24 μm flux of these

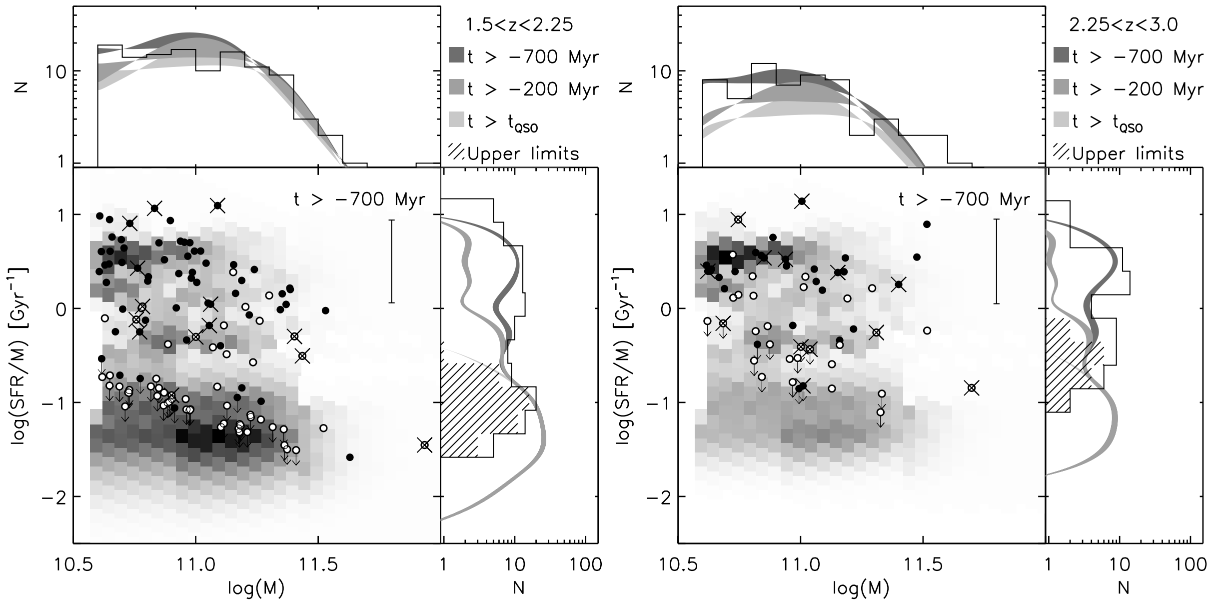

Figure 7.10 — Specific star formation rate as a function of stellar mass for massive galaxies at $1.5 < z < 3$ in the GOODS-South field with colors falling inside (*empty circles*) or outside (*filled circles*) the selection window for quiescent red galaxies. Cross symbols indicate which sources are detected in X-rays. The vertical error bar indicates the systematic error in SFR/M. The model predictions are plotted with greyscales. The top and side panels show the mass and SFR/M distribution, with the black histogram representing the observed sample, and the greyscaled curves showing the model predictions for post-quasars and merging galaxies up to 700, 200, and 0 Myr before the quasar phase. When integrating down to 700 Myr before the quasar phase, the predicted number density of galaxies with $SFR/M > 1$ Gyr^{-1} is 1.6 times smaller than observed, possibly due to AGN contribution to the 24 μm emission from which the observed SFR were derived.

objects could have an AGN contribution. Moreover, Daddi et al. (2007b) recently found that a significant fraction (20-30% to $K_{Vega}^{tot} < 22$, and up to $\sim 50 - 60\%$ for $M \sim 10^{11}\ M_{\odot}$) of star-forming galaxies that are not individually detected in the X-rays show evidence for heavily obscured AGN by the presence of a mid-IR flux excess. The vertical error bar indicates the systematic uncertainty in the conversion from 24 μm flux to the obscured part of the star formation rate. The top and side panels show the distribution of masses and specific star formation rates separately. With lighter polygons, we illustrate how the predicted distribution changes when integrating the merger rate function only to the evaluated redshift or 200 Myr past the evaluated redshift. The latter case includes the nuclear starburst phase, but not earlier star-forming phases.

We conclude that at $1.5 < z < 2.25$ the broad-band color criterion is efficient in distinguishing quiescent from star-forming galaxies with high specific star formation rates. In the higher redshift bin, we are more limited by upper limits on the 24 μm flux. The bulk of broad-band selected quiescent galaxies shows smaller specific star formation rates than their counterparts outside the broad-band selection window, although some reach values above $SFR/M = 1$ Gyr^{-1}.

As in the observations, in particular at $1.5 < z < 2.25$, there is a slight hint that the most heavily star-forming objects reside primarily at the lower masses within our mass-limited sample. Papovich et al. (2006) and Reddy et al. (2006) find that the specific star formation rate is inversely proportional to mass, implying that the ongoing star formation at $z \sim 2$ contributes more significantly to the mass buildup of low-mass galaxies than to high-mass galaxies.

The predicted abundance of merger-triggered nuclear starbursts, occuring between 0 and 200 Myr before the quasar phase, seems to be insufficient to account for all observed massive galaxies with high specific star formation rates ($SFR/M > 1$ Gyr^{-1}). However, when we include earlier phases of star formation induced by the merging event (up to 700 Myr before the quasar phase), we find that the observed number density of galaxies with $SFR/M > 1$ Gyr^{-1} is only a factor 1.6 larger than predicted by the model. Such an offset might be expected from possible AGN contributions to the 24 μm emission from which the star formation rates were derived (see, e.g., Daddi et al. 2007b).

7.9 The abundance of massive galaxies at $1.5 < z < 3$: analysis by type

We now proceed to quantify the observed and modeled number and mass densities of massive galaxies at $1.5 < z < 3$. As before, the model prediction was derived by integrating the merger rate function to include all galaxies that once contributed to the observed quasar luminosity function or will do so in less than 700 Myr. From this, we extracted 4 samples using the tools discussed in §7.7.3 and §7.8: galaxies above $\log M > 10.6$ with broad-band colors satisfying the quiescent red galaxy criterion (Eq. 7.4, §7.9.1), galaxies above $\log M > 10.6$ that do not satisfy Eq. 7.4 (§7.9.2), galaxies with $\log M > 10.6$ and $SFR/M > 1$ Gyr^{-1} (§7.9.3), and finally a sample of galaxies more massive than 10^{11} $M_{\odot}$ with red ($U - V > 1.3$) optical colors (§7.9.4). The last sample allows us to include the larger area MUSYC survey in the comparison, for which no IRAC or MIPS imaging is currently available. In each case, we impose an identical selection criterion on the observed sample of galaxies.

7.9.1 The number and mass density of massive ($\log \mathbf{M} > 10.6$) quiescent red galaxies

Having established the similarity in colors of the model post-quasar population and the observed quiescent red galaxy population above a same mass limit, we now turn to a comparison of their number and mass densities. Our aim is to constrain the fraction (in number and mass) of massive quiescent red galaxies at redshifts $1.5 < z < 3$ that descendants of merger-triggered quasars can account for. In order to do this, we selected the observed and modeled galaxies with $\log M > 10.6$ that lie inside the wedge defined by Eq. 7.4 and compute the number and mass density for the probed comoving volume of $\sim 3.5 \times 10^5$ Mpc^3 in each redshift bin. The resulting number and mass densities are plotted as a function of central redshift of the redshift bin in Figure 7.11(a). The filled circles indicate the observed number and mass density of quiescent red galaxies above $\log M = 10.6$. Their values and corresponding uncertainties are listed in Table 7.1.

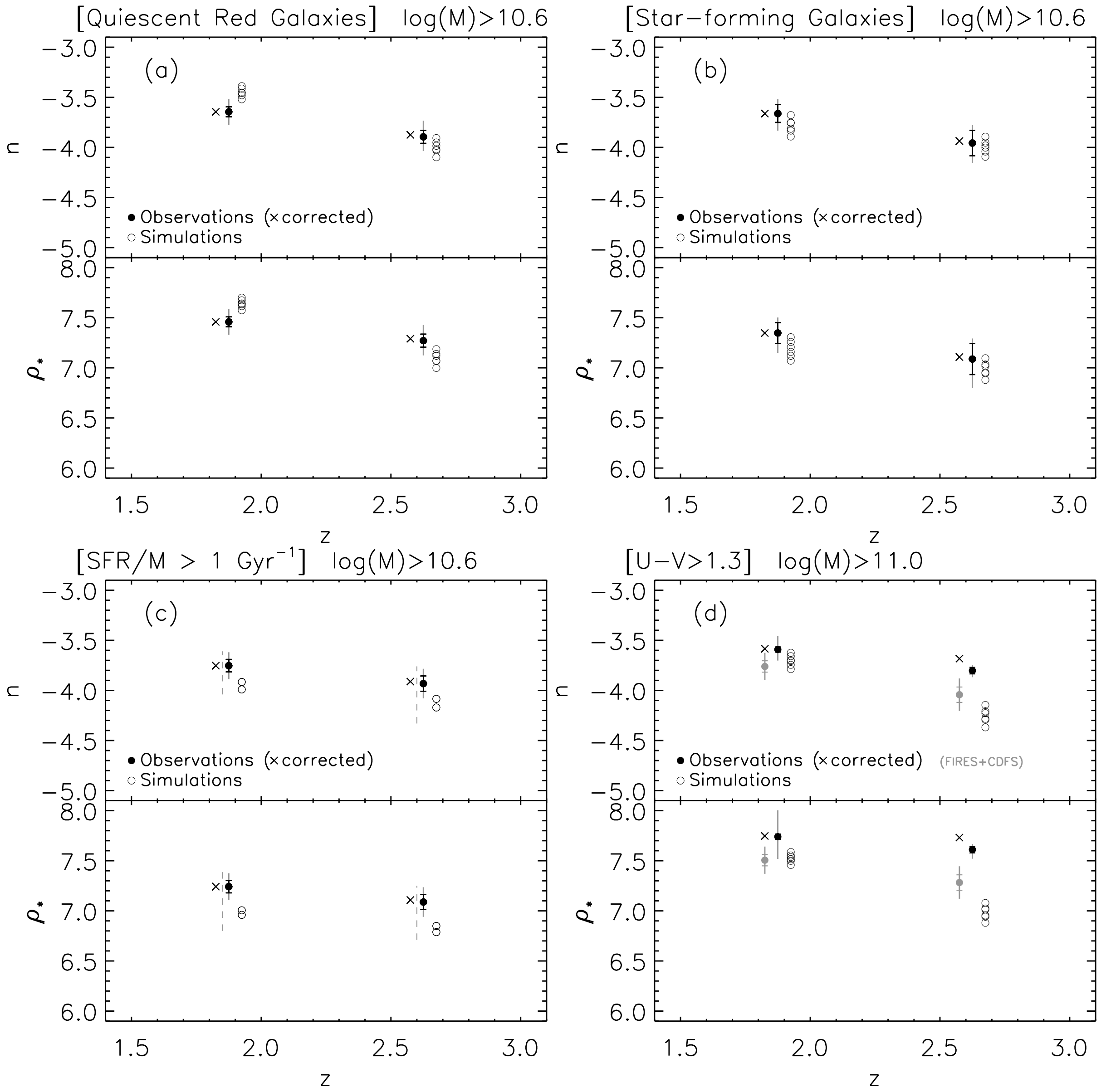

Figure 7.11 — The number and mass density of observed (*filled symbols*) and modeled (*empty symbols*) massive galaxies as a function of redshift above the same mass limit and satisfying the same selection criterion. The cross symbols indicate the observed number and mass density after a correction for incompleteness (which is negligible except for the MUSYC fields). The black error bar represents the Poisson shot noise solely. The grey error bar accounts for uncertainties in redshift, mass, and rest-frame colors and a (mostly dominating) contribution from cosmic variance. The dashed error bar in panel (c) reflects the systematic uncertainty in the SFR. We consider 4 samples: (a) Quiescent red galaxies with $\log M > 10.6$ in FIRES+GOODS-S, (b) Star-forming (non-quiescent) galaxies with $\log M > 10.6$ in FIRES+GOODS-S, (c) galaxies with $SFR/M > 1$ Gyr^{-1} with $\log M > 10.6$ in GOODS-S, and (d) galaxies with $U - V > 1.3$ and $\log M > 11$ in FIRES+GOODS-S+MUSYC. The model predictions were derived by integrating the merger rate function to 700 Myr beyond the evaluated redshift. Changing this value only alters the predictions for panels (b) and (c). We find that both the predicted number and mass densities agree within the error bars with the observed values.

Table 7.1. Number and mass densities for massive galaxies

Type	Mass limit $M_\odot$	Redshift	Observations[a] n 10^{-4} Mpc^{-3}	Observations[a] ρ_* $10^7 M_\odot$ Mpc^{-3}	Model Prediction[b] n 10^{-4} Mpc^{-3}	Model Prediction[b] ρ_* $10^7 M_\odot$ Mpc^{-3}
All	4×10^{10}	$1.5 < z < 2.25$	$4.4^{+1.3}_{-1.0}$	$5.1^{+1.6}_{-1.2}$	$4.8 - 5.6$	$5.6 - 6.3$
All	4×10^{10}	$2.25 < z < 3$	$2.5^{+1.0}_{-0.6}$	$3.2^{+1.5}_{-0.8}$	$1.8 - 2.2$	$2.1 - 2.4$
Quiescent	4×10^{10}	$1.5 < z < 2.25$	$2.3^{+0.8}_{-0.6}$	$2.9^{+1.0}_{-0.7}$	$3.0 - 4.1$	$3.8 - 5.0$
Quiescent	4×10^{10}	$2.25 < z < 3$	$1.3^{+0.6}_{-0.4}$	$2.0^{+0.9}_{-0.6}$	$0.8 - 1.2$	$1.0 - 1.5$
Star-forming	4×10^{10}	$1.5 < z < 2.25$	$2.2^{+0.9}_{-0.7}$	$2.2^{+0.9}_{-0.8}$	$1.3 - 2.1$	$1.2 - 2.0$
Star-forming	4×10^{10}	$2.25 < z < 3$	$1.2^{+0.6}_{-0.4}$	$1.3^{+0.8}_{-0.6}$	$0.8 - 1.3$	$0.8 - 1.2$
$SFR/M > 1$ Gyr^{-1}	4×10^{10}	$1.5 < z < 2.25$	$1.8^{+0.6}_{-0.5}$	$1.7^{+0.6}_{-0.5}$	$1.0 - 1.2$	$0.9 - 1.0$
$SFR/M > 1$ Gyr^{-1}	4×10^{10}	$2.25 < z < 3$	$1.2^{+0.5}_{-0.4}$	$1.3^{+0.5}_{-0.4}$	$0.7 - 0.8$	$0.6 - 0.7$
$U - V > 1.3$	10^{11}	$1.5 < z < 2.25$	$2.6^{+0.9}_{-0.6}$	$5.6^{+4.6}_{-2.2}$	$1.6 - 2.4$	$2.9 - 3.9$
$U - V > 1.3$	10^{11}	$2.25 < z < 3$	$2.1^{+0.3}_{-0.3}$	$5.4^{+0.8}_{-1.0}$	$0.4 - 0.7$	$0.8 - 1.2$

[a] The error bars in the observed densities account for Poisson noise, cosmic variance, and the uncertainties in redshift, rest-frame color and mass of the individual galaxies. They do not account for the systematic dependence on the stellar population synthesis code used to derive the stellar masses, nor was the systematic uncertainty in the conversion from 24 μm to SFR (of the order of 1 dex) included in the results for the sample selected on SFR/M.

[b] The range in model densities indicates a crude estimate of the size of uncertainties in the merger rate function and the dependence on choice of attenuation law and stellar population synthesis code to compute the synthetic photometry.

The cross symbols represent the observed number and mass density after applying a 0% and 5% correction for incompleteness in the low- and high-redshift bin respectively. As in §7.6, the black error bars account for Poisson shot noise. The grey error bars also include selection uncertainties stemming from uncertainties in the redshift, mass, and rest-frame colors of individual galaxies, and a dominating contribution from cosmic variance.

The empty symbols on Figure 7.11(a) indicate the predicted number and mass density of galaxies with $\log M > 10.6$ at $1.5 < z < 2.25$ and $2.25 < z < 3$ whose synthetic photometry places them within the selection wedge for quiescent red galaxies. 95% of these modeled galaxies are in a post-quasar phase of their evolution. The different empty circles represent predictions derived with the BC03 and M05 stellar population synthesis codes, with the Calzetti et al. (2000) attenuation law and the SMC-like attenuation law from Pei (1992). Their spread gives a crude indication of the freedom allowed by the model. It also takes into account the uncertainty in the merger rate function used to place the binary merger simulations in a cosmological context.

We find that in both redshift bins, the observed number and mass density of massive quiescent red galaxies agrees within the error bars with the predicted number and mass density of simulated galaxies satisfying the same selection criterion. In other words, assuming a one-to-one correspondence between quasars and gas-rich mergers, the model by Hopkins et al. (2006b) predicts an abundance of merger remnants (i.e., post-quasar galaxies) that is similar to the observed abundance of quiescent red galaxies. The model predicts an increase by a factor 3.5 in the number and mass density for massive post-quasar galaxies in the 1 Gyr that passed between $z = 2.6$ and $z = 1.9$. The observed sample seems to suggest less evolution (a factor 1.8 in number density and 1.5 in mass density), but is formally consistent with both the factor 3.5 and a non-evolving number and mass density over the considered redshift range.

7.9.2 The number and mass density of massive ($\log \mathbf{M} > \mathbf{10.6}$) star-forming galaxies

Following identical procedures as outlined above, we analyze the number and mass density of massive galaxies with colors outside the quiescent red galaxy wedge in Figure 7.11(b). Again, we used a Monte Carlo simulation to determine how many galaxies move into or out of the selection window when perturbing their properties within the error bars. We took into account the fact that the mass estimates of star-forming galaxies are less robust than for quiescent galaxies. In Chapter 6 we found a typical mass underestimate of -0.1 dex for star-forming galaxies, with the central 68% interval of $\Delta \log M \equiv \log M_{recovered} - \log M_{true}$ ranging from -0.25 to 0 dex.

We find a similar number density of massive quiescent and massive star-forming galaxies in the observed fields. The mass density of the observed star-forming galaxies is lower than that for the quiescent ones above the same mass limit by a factor 1.3 at $z = 1.9$ and 1.5 at $z = 2.6$. We find that the abundances of star-forming galaxies, both in number and mass, as predicted by the merger model agree within the error bars with the observed values. The ratio of quiescent to star-forming galaxies as predicted by the model amounts to 2 (1) for the number density and 2.8 (1.2) for the mass density in the low (high) redshift bin. A more robust model prediction of the pre-quasar number and mass density would also require a careful simulation of the evolutionary stages during which and viewing angles under which the binary merger would be detected as two separate galaxies, thus contributing twice to the number density, but with half the mass and therefore possibly dropping out of the mass-limited sample.

7.9.3 The number and mass density of massive ($\log \mathbf{M} > 10.6$) galaxies with $\mathbf{SFR/M} > 1$ $\mathbf{Gyr^{-1}}$

Selecting galaxies with specific star formation rates above $SFR/M > 1$ Gyr^{-1}, we find an observed number density of 1.8×10^{-4} Mpc^{-3} and 1.2×10^{-4} Mpc^{-3} at $1.5 < z < 2.25$ and $2.25 < z < 3$ respectively (Figure 7.11(c)). Since we interpreted all the 24 μm emission as dust re-emission from star formation, the true number density can be lower depending on the contribution from AGN (see, e.g., Reddy et al. 2005; Papovich et al. 2006; Daddi et al. 2007b). The merger model predicts an abundance of galaxies with high specific star formation rates that is a factor 1.6 smaller than observed. Given the possible AGN contribution to the 24 μm emission and the large systematic uncertainty in the conversion from 24 μm to the dust-obscured contribution to the star formation rate (*dashed line* in Figure 7.11(c)), the model and observational results are formally consistent.

7.9.4 The number and mass density of galaxies with $\mathbf{M} > 10^{11}$ $\mathbf{M}_\odot$ and $\mathbf{U} - \mathbf{V} > 1.3$

In order to reduce the effect of cosmic variance, we now include the MUSYC fields in our analysis, increasing the area by a factor 3 and reducing the cosmic variance with a similar factor. This goes at the cost of depth (the 90% completeness limit for the MUSYC fields is 1 magnitude shallower than for GOODS-South) and wavelength coverage (no IRAC photometry is currently available for the MUSYC fields). Consequently, we are restricted to a sample limited at $M > 10^{11}$ $M_\odot$, even then requiring a 33% correction for incompleteness in the $2.25 < z < 3$ bin. Moreover, the lack of IRAC observations prevents us from selecting galaxies that fall inside the selection window for quiescent red galaxies. We therefore compare the number and mass density of all $M > 10^{11}$ $M_\odot$ galaxies with $U - V > 1.3$ (the lower edge of the quiescent red galaxy wedge), knowing from §7.7 that a significant fraction of the observed galaxies will fall outside the quiescent red galaxy wedge.

Figure 7.11(d) shows their number and mass density as a function of redshift for the combined FIRES, GOODS-South, and MUSYC surveys (*black symbols*). Poisson noise is negligible for this sample. The grey error bars again account for cosmic variance and the uncertainties in redshift, rest-frame color, and mass of the individual galaxies making up the sample. For the MUSYC survey, we assumed an increase in the mass uncertainty by a factor of 3 with respect to the FIRES and GOODS-South samples due to the lack of IRAC photometry (see Wuyts et al. 2007). In contrast to the FIRES + GOODS-South sample discussed above, the total error budget is not always dominated by cosmic variance. The large uncertainty in the mass density at $z \sim 1.9$ for example is mostly attributed to errors in the properties of individual galaxies as derived from the mock catalogs. Separately, we indicate the results obtained from the deeper FIRES and GOODS-South surveys (*grey symbols*, dominated in area by GOODS-South). We conclude that the GOODS-South field is significantly underdense in terms of the highest mass ($M > 10^{11}\ M_\odot$) galaxies, in particular in the $2.25 < z < 3$ redshift bin. Our analysis shows an agreement between the observed abundance (in number and mass) of red ($U - V > 1.3$) massive ($M > 10^{11}\ M_\odot$) galaxies at $1.5 < z < 3$ on the one hand, and the model prediction of galaxies satisfying the same criteria that either had a merger-triggered quasar phase in their past lifetime or will undergo such a phase within 700 Myr on the other hand. In fact, the vast majority of massive red galaxies predicted by the merger model are post-quasar galaxies (see §7.7.3). At $2.25 < z < 3$, the predicted massive post-quasar population can account for at least 25% in number and 20% in mass of the observed massive red galaxy population.

Assuming that the ratio of massive red galaxies ($M > 10^{11}\ M_\odot$ & $U - V > 1.3$) falling inside and outside the quiescent red galaxy selection window in the MUSYC fields equals that in the FIRES and GOODS-South fields, we find that the merger model can account for 70% of the number density and 30% of the mass density of massive quiescent red galaxies at $2.25 < z < 3$ and is consistent with forming all of the massive quiescent red galaxies at $1.5 < z < 2.25$ through mergers involving AGN activity. A recent discussion on the importance of AGN activity at high redshift is provided by Daddi et al. (2007b).

7.10 Comments and caveats

In this section, we list a number of caveats, and indicate prospects for improvements on both the model and observational side. We list a number of possible reasons for the discrepancy between the synthetic and observed colors of massive star-forming galaxies in §7.10.3.

7.10.1 Pair statistics

In this chapter, we used the integrated properties (color, mass, SFR) for the merging pair to predict number and mass densities for different samples of massive galaxies. In other words, we made the approximation that the merging pair is never detected as two separate galaxies. As suggested in §7.9.2, a more detailed modeling should take into account that, depending on the orbital configuration and the viewing angle, this may not always be the case.

The post-quasar predictions are robust, since by that time the two progenitors have formed one galaxy. If at earlier times some of the progenitor pairs are resolved as two separate objects, this will decrease the mass density of massive galaxies since galaxies will drop out of the sample. The effect on the number density is less trivial. On the one hand, galaxies will drop out of the mass-limited sample. On the other hand, some merging pairs will contribute twice. We leave such an extension of the merger model for later work.

Here, we focus on an additional test of the merger model allowed by the fact that some of the pairs will be resolved into two objects. If a large fraction of the massive galaxy population at $1.5 < z < 3$ is indeed related to merging events, as our analysis suggests, we expect to see an excess in the pair statistics with respect to a random distribution of galaxies on the sky.

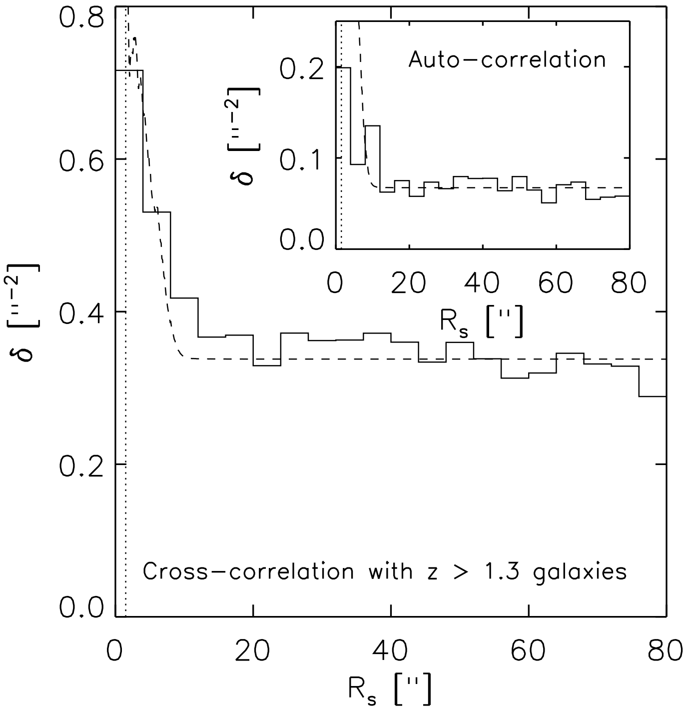

Figure 7.12 — Relative galaxy density (δ) as a function of separation (R_s) between massive ($\log M > 10.6$) $1.5 < z < 3$ galaxies and $z > 1.3$ galaxies in the GOODS-South field. The distribution predicted by the merger model is indicated with the dashed line. At separations smaller than $1\farcs5$ (*dotted line*) an increasing number of galaxy pairs, if present, will be missed because they would be detected as a single object. We find a clear excess at small pair separations ($R_s < 8''$), as predicted by the merger model. A weak pair excess is also visible when only considering the distribution of separations between massive $1.5 < z < 3$ galaxies (*inset panel*), but the excess is much below the prediction.

We present the distribution of galaxy-galaxy separations in the GOODS-South field in Figure 7.12 (*solid histogram*). We decide not to include the other fields, to prevent differences in depth from influencing the pair excess signal. The main panel shows the results from a cross-correlation of our massive ($\log M > 10.6$) galaxy sample at $1.5 < z < 3$ with the sample of all galaxies above $z > 1.3$ in the GOODS-South field, thus avoiding the risk of losing pair members that by a typical photometric redshift error were placed at some lower redshift. For each massive galaxy at $1.5 < z < 3$, we measure the distance to all $z > 1.3$ galaxies. We compute the statistic

$$\delta(R_s) = \frac{\sum_{i=1}^{j} N_i(R_s)}{\pi\left((R_s+\epsilon)^2 + (R_s-\epsilon)^2\right)} \tag{7.5}$$

where j is the total number of objects in our massive galaxy sample and $N_i(R_s)$ is the number of $z > 1.3$ galaxies that lie between a distance $R_s - \epsilon$ and $R_s + \epsilon$ from galaxy i. For a random uniform distribution of galaxies, $\delta(R_s)$ will be flat. Figure 7.12 shows that for our sample of massive galaxies at $1.5 < z < 3$, this is clearly not the case. An excess of pairs at $R_s < 8''$ is visible, also when we consider the distribution of separations between members of the massive galaxy sample at $1.5 < z < 3$ only (*inset panel*).

From the simulations, we measured the physical separations between the 2 merging galaxies and computed the distribution of separation angles in arcseconds on the sky using the merger rate function (see §7.5). Adding the mean value of δ as measured in the interval $30'' < R_s < 80''$, we obtain a model prediction (*dashed line*) that is in qualitative agreement with the cross-correlation results, but larger than the weak pair excess seen in the auto-correlation. Admittedly, the predicted distribution is subject to the orbital configuration set at the start of the simulation, an effect that is not explored in this chapter.

7.10.2 Dependence on stellar population synthesis code

As pointed out in §7.9.1, the predicted rest-frame NIR luminosities for a single stellar population of a given mass are brighter for the M05 than for the BC03 stellar population synthesis code. Consequently, the mass estimates for observed galaxies with ages between 0.2 and 2 Gyr are lower by about a factor 1.5 when modeled with M05 instead of BC03 templates. We indicated the resulting systematic uncertainties in the number and mass densities of the modeled post-quasar galaxy population. This systematic uncertainty is also present in the estimates of number and mass density for the observations, for which so far we only included the formal uncertainties in mass obtained with BC03 SED modeling. To quantify the impact on the derived number and mass densities, we simply divide all stellar masses by 1.5 and repeat the selection procedure and the calculation of the densities. Using this crude approach, we find number densities for all samples discussed in this chapter to be 50-80% and mass densities to be 40-60% of the value obtained with BC03 masses. Although a significant source of uncertainty, we find that for most samples discussed in this chapter (except for the quiescent red galaxy sample at $z \sim 1.9$) adopting the M05 mass estimates would only improve the agreement between data and model. Finally, deviations from a Salpeter (1955) IMF would change our results on number and mass densities of massive galaxies, but in a similar manner for the observations and the simulations, thus keeping intact the relative trends.

7.10.3 Reproducing dusty red starbursts

As discussed in §7.7.3.2, the synthetic colors during the star-forming phases of the merger do not reproduce the red optical and optical-to-NIR colors observed for dusty starbursts. If the lack of model colors redder than $V - J > 1.8$ could be fixed, the statistics based on the merger model, when compared to the observed abundances of massive galaxies, strengthen the idea that the model gives a valid representation of galaxy evolution in the real universe. Here we list a number of possible origins for the discrepancy in colors. Future investigations along these lines will help to further test the merger model.

7.10.3.1 Simulating the observing procedure

First, it is possible that the colors of observed and modeled galaxies are in fact in agreement, but that a discrepancy was found because we did not simulate the whole observing procedure. The observed colors are measured on PSF-matched images within apertures of size 1″ to 2″, whereas the synthetic colors were based on integrated photometry of all stellar particles, irrespective of their location. The presence of a color gradient with redder emission in the central regions of the galaxies could therefore induce an offset in colors in the observed direction.

7.10.3.2 Stellar population synthesis

Second, the discrepancy in colors could be real, but due to an incorrect modeling of the stellar populations, rather than invalid assumptions at the basis of the model (i.e., the one-to-one correspondence between quasars and gas-rich mergers). Apart from the choice of stellar population synthesis code (see §7.10.2), the synthetic photometry depends on the attenuation law applied to each of the stellar particles. We note however that the use of a Milky Way-like attenuation law from Pei (1992) leads to colors intermediate between those based on the Calzetti et al. (2000) and SMC-like (Pei 1992) attenuation laws presented in this chapter. An attenuation law that is less grey than that of the SMC would be required to reproduce the red colors of dusty starburst galaxies.

Another stellar population parameter influencing the synthetic colors is the metallicity of the gas and the stars. In this chapter, we adopted initial gas metallicities derived from the closed box model (Talbot & Arnett 1971) for the 80% gas fraction (f_{gas}) at the start of the simulation:

$$Z_{init} = -y \ln(f_{gas}) \tag{7.6}$$

where $y = 0.02$ is the yield. The simulation keeps track of the subsequent evolution in the gas metallicity, and stellar metallicities are based on the metallicity of the gas out of which they form. If the gas was pre-enriched, this would boost the optical depths and redden the colors. Evidence of high ($\sim Z_{\odot}$) metallicities of massive high-redshift galaxies with red colors is given by van Dokkum et al. (2004). Repeating the post-processing of simulation snapshots with $1Z_{\odot}$ added to the gas and stellar metallicities, we obtain colors that are 0.2 to 0.5 mag redder in $U - V$ and 0.3 to 1.1 mag redder in $V - J$. We note however that in $V - J$ the largest increase occurs for blue galaxies and the color distribution based on BC03 does not reach beyond $V - J \sim 2$.

7.10.3.3 Merger parameters

Third, the discrepancy in colors might imply that the simulations are not characteristic for the merger activity occuring in the real universe. Hopkins et al. (2006b) confirmed the robustness of the model for quasar lifetimes and the derived merger rate function against changes in various parameters of the merging galaxies, such as gas fraction, orbital parameters and changes in the mass ratio of the progenitors (considering 1:1, 2:1, 3:1, and 5:1 mass ratios). All of the simulations used in this work are equal-mass gas-rich ($f_{gas} = 0.8$) mergers. A smaller initial gas fraction would mean that a larger fraction of the stars was already formed before the merger-triggered starburst. This leads to slightly redder $U - V$ colors. Considering earlier stages in the evolutionary scenario, Dasyra et al. (2006) find for a population of local ULIRGs that still have 2 distinct nuclei that the typical mass fraction is 1.5:1, close to equal-mass mergers. In order to extend the model predictions to lower masses, a detailed study of minor merger simulations will be required to determine the minimum mass ratio required to trigger a (low-luminosity) quasar phase.

7.10.3.4 Evolutionary history

Fourth, it is possible that dusty starburst galaxies are not triggered by mergers, but had a different evolutionary history. Daddi et al. (2007a) make this claim based on the long star formation timescales of ULIRGs at high redshift.

7.10.3.5 Mass loss and intergalactic environment

Fifth, gas replenishment from mass loss and infall of gas from the intergalactic environment could change the optical depths and thus the reddening factors. The simulations only take into account a small amount of mass loss: 10% of the gas mass converted into stars is instantaneously returned to the interstellar medium, accounting for short-lived stars that die as supernovae (Springel & Hernquist 2003). The total fraction of the mass lost by a single stellar population with Salpeter (1955) IMF amounts to $\sim 70\%$ (BC03) and is even higher for the top-heavy IMFs of Kroupa (2001) or Chabrier (2003). Furthermore, the simulations do not allow for infall of primordial gas at later times. Consequently, they cannot prove that descendants of galaxies that once showed up in the quasar luminosity function and after the shutdown of star formation reached red colors, will remain quiescent forever. Small amounts of newly accreted gas triggering star formation may be enough to shift a post-quasar galaxy outside the quiescent region of color-color space defined by Eq. 7.4, thus dropping their contribution to the observed galaxy population of massive quiescent red galaxies. Cosmological simulations at sufficient resolution might resolve this problem. At the very least, it would be interesting to test the behavior of simulated merger remnants hosting a supermassive black hole when a small but continuous gas supply is applied.

7.10.3.6 Dust distribution

Finally, the distribution of dust in the simulated galaxies might not reflect reality. A more efficient reddening would be obtained if a foreground screen of obscuring material were present. One possible mechanism that could produce such a configuration is a large-scale wind. The GADGET-2 code (Springel 2005b) used to run the simulations in principle allows for such a phenomenon, but an investigation of the velocity field of the gas in the simulations is required to check whether such a wind is effectively taking place.

7.10.4 Cosmic variance

From the observational side, cosmic variance is the dominant source of uncertainty for the determination of the number and mass density of massive quiescent galaxies. IRAC photometry over a MUSYC area and to a similar depth as FIRES and GOODS-South would be required to further constrain the fraction of massive quiescent galaxies that post-quasar galaxies can account for.

7.11 Summary

We confronted the model by Hopkins et al. (2006b) with observations of massive galaxies at $1.5 < z < 3$. The model translates the observed quasar luminosity function into the abundance of massive merging galaxies and merger remnants. We derived the synthetic photometry for these systems from a set of binary merger SPH simulations with a range of masses, and including stellar and AGN feedback. We extracted mass-limited samples of $1.5 < z < 3$ galaxies with $M > 4 \times 10^{10}\ M_\odot$ and $M > 10^{11}\ M_\odot$ from the FIRES+GOODS-South and FIRES+GOODS-South+MUSYC surveys respectively. We tested the model by comparing the predicted number and mass densities, and the $U - V$ and $V - J$ color distributions with our observations of massive galaxies at $1.5 < z < 3$.

We find that the overall number density of galaxies with $M > 4 \times 10^{10}\ M_\odot$ in the FIRES and GOODS-South fields ($n = 4.4^{+1.3}_{-1.0} \times 10^{-4}$ Mpc^{-3} at $z \sim 1.9$ and $n = 2.5^{+1.0}_{-0.6} \times 10^{-4}$ Mpc^{-3} at $z \sim 2.6$) is in good agreement with the model prediction ($n = 4.8 - 5.6 \times 10^{-4}$ Mpc^{-3} at $z \sim 1.9$ and $n = 1.8 - 2.2 \times 10^{-4}$ Mpc^{-3} at $z \sim 2.6$). Likewise, the results obtained for the mass density are consistent: $\rho_* = 5.1^{+1.6}_{-1.2} \times 10^7\ M_\odot$ Mpc^{-3} at $z \sim 1.9$ and $\rho_* = 3.2^{+1.5}_{-0.8} \times 10^7\ M_\odot$ Mpc^{-3} at $z \sim 2.6$ for the observations and $\rho_* = 5.6 - 6.3 \times 10^7\ M_\odot$ Mpc^{-3} at $z \sim 1.9$ and $\rho_* = 2.1 - 2.4 \times 10^7\ M_\odot$ Mpc^{-3} at $z \sim 2.6$.

Separating massive galaxies by type, we find that the model photometry of the post-quasar population coincides with the region of $U - V$ versus $V - J$ color-color space that was defined by Labbé et al. (in preparation) to select quiescent red galaxies. The observed and modeled number and mass densities of massive ($M > 4 \times 10^{10}\ M_\odot$) quiescent red galaxies at $1.5 < z < 3$ are consistent within the error bars (see Table 7.1).

We added the MUSYC survey to our sample, increasing the area by a factor of 3, but by lack of IRAC data loosing the ability to break at least partially the age-dust degeneracy. As pointed out earlier by van Dokkum et al. (2006), the GOODS-South field is underdense in the $1.5 < z < 3$ redshift interval. Based on the FIRES+GOODS-South+MUSYC sample, we find that more than 25% of the $z \sim 2.6$ galaxies with $M > 10^{11}\ M_\odot$ and $U - V > 1.3$ and essentially all of the $z \sim 1.9$ galaxies satisfying the same criteria can be accounted for by the predicted post-quasar population. The fraction of observed quiescent galaxies at $z \sim 2.6$ that the model can account for increases if we use Maraston (2005) models to derive stellar masses for our observed galaxy sample.

Although less constrained, the predicted abundances of galaxies with star formation triggered by merging and galaxies with $SFR/M > 1$ Gyr^{-1} during the merging phases are also consistent with the observations. However, the predicted color distribution of star-forming galaxies does not match the observations. In particular the colors of red ($V - J > 1.8$) dusty starburst galaxies are not reproduced. We suggest a number of explanations for the lack of dusty red starburst galaxies in the model predictions. Possible reasons are an incomplete simulation of the observing procedure, differences in stellar population properties or merger characteristics between the observed and simulated galaxies, a different history for dusty starbursts than a merger-triggered scenario, additional gas (and dust) from the intergalactic environment or mass loss, and a different distribution of the dust, e.g., caused by the presence of large-scale outflows.

Finally, we find a pair excess at small angular scales, further strengthening the hypothesis that mergers play a key role in galaxy evolution.

Acknowledgments

We would like to thank the Institute for Theory and Computation for its hospitality during several working visits, and the Leids Kerkhoven-Bosscha Fonds for the generous travel support.

References

Adelberger, K. L., Steidel, C. C., Shapley, A. E., Hunt, M. P., Erb, D. K., Reddy, N. A.,& Pettini, M. 2004, ApJ, 607, 226

Bolzonella, M., Miralles, J.-M.,& Pelló, R. 2000, A&A, 363, 476

Bower, R. G., Benson, A. J., Malbon, R., Helly, J. C., Frenk, C. S., Baugh, C. M., Cole, S.,& Lacey, C. G. 2006, MNRAS, 370, 654

Calzetti, D., et al. 2000, ApJ, 533, 682

Chabrier, G. 2003, ApJ, 586, L133

Cowie, L. L., Songaila, A., Hu, E. M.,& Cohen, J. G. 1996, AJ, 112, 839

Cox, T. J., Dutta, S. N., Di Matteo, T., Hernquist, L., Hopkins, P. F., Robertson, B.,& Springel, V. 2006, ApJ, 650, 791

Croton, D. J. et al. 2006, MNRAS, 367, 864

Daddi, E., Cimatti, A., Renzini, A., Fontana, A., Mignoli, M., Pozzetti, L., Tozzi, P.,& Zamorani, G. 2004, ApJ, 617, 746

Daddi, E., et al. 2007a, astro-ph/07052831

Daddi, E., et al. 2007b, astro-ph/07052832

Dasyra, K. M., Tacconi, L. J., Davies, R. I., Genzel, R., Lutz, D., Naab, T., Burkert, A., Veilleux, S.,& Sanders, D. B. 2006, ApJ, 638, 745

De Lucia, G.,& Blaizot, J. 2007, MNRAS, 375, 2

Di Matteo, T., Springel, V.,& Hernquist, L. 2005, Nature, 433, 604

Erb, D. K., Steidel, C. C., Shapley, A. E., Pettini, M., Reddy, N. A.,& Adelberger, K. L. 2006, ApJ, 646, 107

Ferrarese, L.,& Merritt, D. 2000, ApJ, 539, L9

Förster Schreiber, N. M., et al. 2006, AJ, 131, 1891

Franx, M., et al. 2000, The Messenger 99, pp. 20-22

Franx, M., et al. 2003, ApJ, 587, L79

Gebhardt, K., et al. 2000, ApJ, 539, L13

Giavalisco, M.,& the GOODS Team 2004, ApJ, 600, L93

Gingold, R. A.,& Monaghan, J. J. 1977, MNRAS, 181, 375

Granato G. L., De Zotti, G., Silva, L., Bressan, A.,& Danese, L. 2004, ApJ, 600, 580

Hasinger, G., Miyaji, T.,& Schmidt, M. 2005, A&A, 441, 417

Hopkins, P. F., Hernquist, L., Cox, T. J., Di Matteo, T., Robertson, B.,& Springel, V. 2006a, ApJS, 163, 1

Hopkins, P. F., Hernquist, L., Cox, T. J., Robertson, B.,& Springel, V. 2006b, ApJS, 163, 50

Hopkins, P. F., Hernquist, L., Cox, T. J., Robertson, B.,& Krause, E. 2007, astro-ph/0701351

Kriek, M., et al. 2006, ApJ, 649, 71

Kroupa, P. 2001, MNRAS, 322, 231

Labbé, I., et al. 2003, AJ, 125, 1107

Labbé, I., et al. 2005, ApJ, 624, L81

Li, Y., et al. 2006, astro-ph/0608190

Lucy, L. B. 1977, AJ, 82, 1013

Magorrian, J., et al. 1998, AJ, 115, 2285

Maraston, C. 2005, MNRAS, 362, 799

Maraston, C., Daddi, E., Renzini, A., Cimatti, A., Dickinson, M., Papovich, C., Pasquali, A.,& Pirzkal, N. 2006, ApJ, 652, 85

Papovich, C., et al. 2006, ApJ, 640, 92

Pei, Y. C. 1992, ApJ, 395, 130

Pettini, M., Kellogg, M., Steidel, C. C., Dickinson, M., Adelberger, K. L.,& Giavalisco, M. 1998, ApJ, 508, 539

Pettini, M., et al. 2001, ApJ, 554, 981
Quadri, R., et al. 2007, ApJ, 654, 138
Reddy, N. A., Erb, D. K., Steidel, C. C., Shapley, A. E., Adelberger, K. L.,& Pettini, M. 2005, ApJ, 633, 748
Reddy, N. A., et al. 2006, ApJ, 644, 792
Richards, G. T., et al. 2005, MNRAS, 360, 839
Robertson, B., Cox, T. J., Hernquist, L., Franx, M., Hopkins, P. F., Martini, P.,& Springel, V. 2006, ApJ, 641, 21
Rudnick, G., et al. 2001, AJ, 122, 2205
Rudnick, G., et al. 2003, ApJ, 599, 847
Sanders, D. B., Soifer, B. T., Elias, J. H., Madore, B. F., Matthews, K., Neugebauer, G.,& Scoville, N. Z. 1988, ApJ, 325, 74
Shapley, A. E., Steidel, C. C., Pettini, M.,& Adelberger, K. L. 2003, ApJ, 588, 65
Somerville, R. S. 2004, in Multiwavelength mapping of galaxy formation and evolution, ed. R. Bender,& A. Renzini (Berlin: Springer) (astro-ph/0401570)
Somerville, R. S., Lee, K., Ferguson, H. C., Gardner, J. P., Moustakas, L. A.,& Giavalisco, M. 2004, ApJ, L171
Springel, V.,& Hernquist, L. 2003, MNRAS, 339, 289
Springel, V., Di Matteo, T.,& Hernquist, L. 2005a, ApJ, 620, L79
Springel, V., Di Matteo, T.,& Hernquist, L. 2005b, MNRAS, 361, 776
Steidel, C. C., Adelberger, K. L., Shapley, A. E., Pettini, M., Dickinson, M.,& Giavalisco, M. 2003, ApJ, 592, 728
Talbot, R. J,& Arnett, W. D., 1971, ApJ, 170, 409
Ueda, Y., Akiyama, M., Ohta, K.,& Miyaji, T. 2003, ApJ, 598, 886
van der Wel, A., Franx, M., Wuyts, S., van Dokkum, P. G., Huang, J., Rix, H.-W.,& Illingworth, G. D. 2006, ApJ, 652, 97
van Dokkum, P. G., et al. 2004, ApJ, 611, 703
van Dokkum, P. G., Kriek, M., Rodgers, B., Franx, M.,& Puxley, P. 2005, ApJ, 622, L13
van Dokkum, P. G., et al. 2006, ApJ, 638, 59
Wuyts, S., et al. 2007, ApJ, 655, 51
Yan, H. et al. 2004, ApJ, 616, 63